Examination of aerosol impacts on convective clouds and precipitation in two metropolitan areas in East Asia; how varying depths of convective clouds between the areas diversify those aerosol effects?

Seoung Soo Lee[1,2], Jinho Choi[3], Goun Kim[4], Kyung-Ja Ha[2,5,6], Kyong-Hwan Seo[3], Chang-Hoon Jung[7], Junshik Um[3], Youtong Zheng[8], Jianping Guo[9]

[1]Earth System Science Interdisciplinary Center, University of Maryland, Maryland

[2]Research Center for Climate Sciences, Pusan National University, Busan, Republic of Korea

[3]Department of Atmospheric Sciences, Division of Earth Environmental System, Pusan National University, Busan, Republic of Korea

[4]Marine Disaster Research Center, Korea Institute of Ocean Science and Technology, Pusan, Republic of Korea

[5]Center for Climate Physics, Institute for Basic Science, Busan, Republic of Korea

[6]BK21 School of Earth and Environmental Systems, Pusan National University, Busan, Republic of Korea

[7]Department of Health Management, Kyungin Women's University, Incheon, Republic of Korea

[8]The Program in Atmospheric and Oceanic Sciences, Princeton University, and National Oceanic and Atmospheric Administration/Geophysical Fluid Dynamics Laboratory, Princeton, New Jersey, USA

[9]State Key Laboratory of Severe Weather, Chinese Academy of Meteorological Sciences, Beijing, China

Corresponding author: Seoung Soo Lee
Office: (303) 497-6615
Fax: (303) 497-5318
E-mail: cumulss@gmail.com, slee1247@umd.edu

Abstract

This study examines the role played by aerosols which act as cloud condensation nuclei (CCN) in the development of clouds and precipitation in two metropolitan areas in East Asia that have experienced substantial increases in aerosol concentrations over the last decades. These two areas are the Seoul and Beijing areas and the examination has been done by performing simulations using the Advanced Research Weather Research and Forecasting model as a cloud-system resolving model. CCN are advected from the continent to the Seoul area and this increases aerosol concentrations in the Seoul area. These increased CCN concentrations induce the enhancement of condensation that in turn induces the enhancement of deposition and precipitation amount in a system of less deep convective clouds as compared to those in the Beijing area. In a system of deeper clouds in the Beijing area, increasing CCN concentrations also enhance condensation but reduce deposition. This leads to CCN-induced negligible changes in precipitation amount. Also, in the system, there is a competition for convective energy among clouds with different condensation and updrafts. This competition results in different responses to increasing CCN concentrations among different types of precipitation, which are light, medium and heavy precipitation in the Beijing area. CCN-induced changes in freezing play a negligible role in CCN-precipitation interactions as compared to the role played by CCN-induced changes in condensation and deposition in both of the areas.

1. Introduction

With increasing aerosol loading or concentrations, cloud-particle sizes can be changed. In general, with increasing droplet sizes, the efficiency of collision and collection among droplets increases. Increasing aerosol loading is known to make the droplet size smaller and thus make the efficiency of collision and collection among droplets lower. This leads to less droplets or cloud liquid forming raindrops and there is more cloud liquid present in the air to be evaporated or frozen. Studies have shown that increases in cloud-liquid mass due to increasing aerosol loading can enhance the freezing of cloud liquid and parcel buoyancy, which lead to the invigoration of convection (Rosenfeld et al., 2008; Fan et al., 2009). Via the invigoration of convection, precipitation can be enhanced. The dependence of aerosol-induced invigoration of convection and precipitation enhancement on aerosol-induced increases in condensational heating in the warm sector of a cloud system has been shown (e.g., van den Heever et al., 2006; Fan et al., 2009; Lee et al., 2018). Increasing cloud-liquid mass induces increasing evaporation, which intensifies gust fronts. This in turn strengthens convective clouds and increases the amount of precipitation (Khain et al., 2005; Tao et al., 2007; Storer et al., 2010; Tao et al., 2012; Lee et al., 2017; Lee et al., 2018). It is notable that aerosol-induced precipitation enhancement is strongly sensitive to cloud types that can be defined by cloud characteristics such as cloud depth (e.g., Tao et al., 2007; Lee et al., 2008; Fan et al., 2009).

Since East Asia was industrialized, there have been substantial increases in aerosol concentrations over the last decades in East Asia (e.g., Lee et al., 2013; Lu et al., 2011; Oh et al., 2015; Dong et al., 2019). These increases are far greater than those in other regions such as North America and Europe (e.g., Lu et al., 2011; Dong et al., 2019). While those increasing aerosols affect clouds, precipitation and hydrologic circulations in the continental East Asia, the increase in the advected aerosols from the continent to the Korean Peninsula affect clouds, precipitation and hydrologic circulations in the Korean Peninsula (Kar et al., 2009). This study aims to examine effects of the increasing aerosols, which particularly act as cloud condensation nuclei (CCN), and their advection on clouds and precipitation in East Asia. This study focuses on aerosols which act as CCN, but not ice-nucleating particles (INPs), to examine those effects, based on the fact that CCN

account for most of aerosol mass that affects clouds and precipitation, and CCN, but not INPs, are associated with above-described aerosol-induced invigoration of convection and intensification of gust fronts. Note that these aerosol-induced invigoration and intensification are two well-established major theories of aerosol-cloud interactions. As a first step to the examination, this study focuses on two metropolitan areas in East Asia which are the Beijing and Seoul areas. The population of each of the Beijing and Seoul areas is ~ 20 millions. Associated with this, these areas have lots of aerosol sources (e.g., traffic) and have made a substantial contribution to the increases in aerosol concentrations in East Asia. Hence, we believe that these two cities can represent overall situations related to increasing aerosol concentrations in East Asia.

As mentioned above, aerosol-cloud interactions (and their impacts on precipitation) are strongly dependent on cloud types and thus to gain a more general understanding of those interactions, we select cases from the Beijing and Seoul areas with different cloud types. A selected case from the Beijing area involves deep convective clouds that reach the tropopause, while a selected case from the Seoul area involves comparatively shallow (or less deep) convective clouds. Via comparisons between these two cases, we aim to identify mechanisms that control varying aerosol-cloud interactions with cloud types.

To examine impacts of aerosols, which act as CCN, on clouds and precipitation in the cases, numerical simulations are performed, as a way of fulfilling above-described aim. These simulations use a cloud-system resolving model (CSRM) that has reasonably high resolutions to resolve cloud-scale processes that are related to cloud microphysics and dynamics. Hence, these simulations are able to find process-level mechanisms in association with cloud-scale processes.

2. Case description

In the Seoul area, South Korea, there is an observed mesoscale convective system (MCS) for a period from 03:00 LST (local solar time) to 18:00 LST December 24th 2017. During this period, there is a recorded moderate amount of precipitation and its maximum precipitation rate reaches ~ 13 mm hr^{-1}. Here, precipitation in the Seoul area is measured by rain gauges in automatic weather stations (AWSs) (King, 2009). The measurement is

145 performed hourly with a spatial resolution that ranges from ~1 km to ~10 km. The Seoul
146 area is marked by an inner rectangle in Figure 1a and Figure 2a and dots in the rectangle
147 in Figure 2a mark the selected locations of rain gauges. At 21:00 LST December 23rd 2017,
148 synoptic-scale features develop in favor of the formation and development of the selected
149 MCS and associated moderate rainfall. A low-pressure trough was over northeast China
150 and the Yellow Sea (Figure 1a). Along the flank of the low-pressure system, there was the
151 southwesterly low-level jets to transport warm and moist air. This warm and moist air is
152 originated from the Yellow Sea and transported to the Korean Peninsula (Figure 1a). The
153 southwesterly low-level jet plays an important role in the formation and development of
154 rainfall events in the Korean Peninsula by fetching warm and moist air (Hwang and Lee
155 1993; Lee et al. 1998; Seo et al. 2013; Oh et al. 2018).
156 There was another observed MCS case in the Beijing area, China for a period from
157 14:00 LST on July 27th to 00:00 LST July 28th 2015. There is a substantial recorded amount
158 of precipitation for this period and its maximum precipitation rate reaches ~ 45 mm hr^{-1}.
159 Here, similar to the situation in the Seoul area, precipitation in the Beijing area is measured
160 by rain gauges in AWSs hourly with a spatial resolution that ranges from ~1 km to ~10 km.
161 The Beijing area is marked by an inner rectangle in Figure 1b and Figure 2b and dots in
162 the rectangle in Figure 2b mark the selected locations of rain gauges. At 09:00 LST July
163 27th 2015, synoptic-scale features develop in favor of the formation and development of
164 the selected MCS. The southerly low-level jet forms and develops heavy rainfall events in
165 the Beijing area by transporting warm and moist air to the area (Figure 1b). Note that
166 synoptic features in Figures 1a and 1b are based on reanalysis data that are produced by
167 the Met Office Unified Model (Brown et al., 2012) every 6 hours with a 0.11° × 0.11°
168 resolution.
169
170 **3. CSRM and simulations**
171
172 **3.1 CSRM**
173
174 The Advanced Research Weather Research and Forecasting (ARW) model (version 3.3.1)
175 is used as a CSRM. The ARW model is a compressible model with a nonhydrostatic status.

A 5th-order monotonic advection scheme is used to advect microphysical variables (Wang et al., 2009). The Rapid Radiation Transfer Model (RRTMG; Mlawer et al., 1997; Fouquart and Bonnel, 1980) is adopted to parameterize shortwave and longwave radiation in simulations. A microphysics scheme that is used in this study calculates the effective sizes of hydrometeors that are fed into the RRTMG, and the RRTMG simulates how these effective sizes affect radiation.

The CSRM adopts a bin scheme as a way of parameterizing microphysics. The Hebrew University Cloud Model (HUCM) detailed in Khain et al. (2011) is the bin scheme. A set of kinetic equations is solved by the bin scheme to represent size distribution functions for each class of hydrometeors and aerosols acting as CCN. The hydrometeor classes are water drops, ice crystals (plate, columnar and branch types), snow aggregates, graupel and hail. Drops whose radius is smaller (larger) than 40 μm are categorized to be droplets (raindrops). There are 33 bins for each size distribution in a way that the mass of a particle m_j in the j bin is to be $m_j = 2m_{j-1}$.

A cloud-droplet nucleation parameterization based on Köhler theory represents cloud-droplet nucleation. Arbitrary aerosol mixing states and aerosol size distributions can be fed to this parameterization. To represent heterogeneous ice-crystal nucleation, parameterizations by Lohmann and Diehl (2006) and Möhler et al. (2006) are used. In these parameterizations, contact, immersion, condensation-freezing, and deposition nucleation paths are all considered by taking into account the size distribution of INPs, temperature and supersaturation. Homogeneous droplet freezing is considered following the theory developed by Koop et al. (2000).

3.2 Control runs

For a three-dimensional CSRM simulation of the observed case of convective clouds in the Seoul (Beijing) area, i.e., the control-s (control-b) run, a domain just over the Seoul (Beijing) area, which is shown in Figure 1a (1b) and Figure 2a (2b), is used. This domain adopts a 300-m resolution. The control-s run is for a period from 03:00 LST to18:00 LST December 24th 2017, while the control-b run is for a period from 14:00 LST on July 27th to 00:00 LST July 28th 2015. The length of the domain is 170 (140) km in the east-west

(north-south) direction for the control-s run, and 280 (240) km for the control-b run. There are 100 vertical layers and these layers employ a sigma coordinate that follows the terrain. The top pressure of the model is 50 hPa for both of the control-s and control-b runs. On average, the vertical resolution is ~200 m.

Reanalysis data, which are produced by the Met Office Unified Model, represent the synoptic-scale features, provide initial and boundary conditions of variables such as wind, potential temperature, and specific humidity for the simulations. The simulations adopt an open lateral boundary condition. The Noah land surface model (LSM; Chen and Dudhia, 2001) calculates surface heat fluxes.

The current version of the ARW model is not able to consider the spatiotemporal variation of aerosol properties. In order to take into account the spatiotemporal variation of aerosol properties, which is typical in metropolitan areas, such as composition and number concentration, an aerosol preprocessor, which is able to consider the variability of aerosol properties, is developed and used in the simulations. This aerosol preprocessor interpolates or extrapolates background aerosol properties in observation data such as aerosol mass (e.g., $PM_{2.5}$ and PM_{10}) into grid points and time steps in the model. In this study, the inverse distance weighting method is used for the extrapolation and interpolation of observation data including aerosol mass into grid points and time steps in the model. PM stands for particulate matter. The mass of aerosols with diameter smaller than 2.5 (10.0) μm per unit volume of the air is $PM_{2.5}$ (PM_{10}).

$PM_{2.5}$ or PM_{10}, which are measured by surface observation sites in the domains, is used to consider the variability of aerosol properties. The distance between the observation sites ranges from ~1 km to ~10 km and the time interval between observations of aerosol mass is ~ 10 minutes; the selected locations of these sites are marked by dots in the inner rectangles in Figure 2. Hence, the variability is represented by fine spatiotemporal resolutions of the sites. The ground sites that are equipped with the aerosol robotic network (AERONET; Holben et al., 2001) are in the domains. Distances between these sites are ~10 km. In this study, $PM_{2.5}$/PM_{10} data are used to represent the spatiotemporal variability of aerosols over the domains and the simulation periods. To represent aerosol composition and size distributions, data from the AERONET sites are employed.

The AERONET data are averaged over the AERONET sites at 02:00 LST December 24th 2017 (13:00 LST July 27th 2015), which is 1 hour before the observed MCS forms, for the Seoul (Beijing) case. Based on the average data, it is assumed that aerosol particles are internally mixed with 70 (80) % ammonium sulfate and 30 (20) % organic compound for the Seoul (Beijing) case. This mixture is assumed to represent aerosol chemical composition in the whole domain and during the entire simulation period. Since ammonium sulfate and organic compound are representative components of CCN, it is assumed that the mass of aerosols that act as CCN is represented by $PM_{2.5}$ and PM_{10} for the Seoul and Beijing areas, respectively. Aerosols reflect, scatter and absorb shortwave and longwave radiation before they are activated. This type of aerosol-radiation interactions is not taken into account in this study. This is mainly based on the fact that in the mixture, there is insignificant amount of radiation absorbers; black carbon is a representative radiation absorber. The AERONET observation indicates that the size distribution of background aerosols acting as CCN follows the tri-modal log-normal distribution for the Seoul (Beijing) case as exemplified in Figure 3a (3b). It is assumed that for the whole domain and simulation period, the size distribution of background aerosols acting as CCN follows the shape of distribution with specific size distribution parameters (i.e., modal radius and standard deviation of each of Aitken, accumulation and coarse modes, and the partition of aerosol number among those modes) as shown in Figure 3a (3b) for the Seoul (Beijing) case. Modal radius of the shape of distribution is 0.015 (0.012), 0.110 (0.085), and 1.413 (1.523) μm, while standard deviation of the shape of distribution is 1.28 (1.10), 1.54 (1.63), and 1.75 (1.73) for Aitken, accumulation and coarse modes, respectively, in the Seoul (Beijing) case. The partition of aerosol number, which is normalized by the total aerosol number of the size distribution, is 0.555 (0.612), 0.444 (0.387), and 0.001 (0.001) for Aitken, accumulation and coarse modes, respectively, in the Seoul (Beijing) case. The distribution parameters of the assumed shape of the size distribution of background aerosols in Figure 3a (3b) are those that are averaged over the AERONET sites at a time point, which is 1 hour before the observed MCS form, for the Seoul (Beijing) case. By using $PM_{2.5}$ or PM_{10}, which is interpolated and extrapolated to grid points immediately above the surface and time steps, and based on the assumption of aerosol composition and size distribution above, the background number concentrations of aerosols acting as CCN

are obtained for the simulation for each of the cases. There is no variation with height in background concentrations of aerosols acting as CCN from immediately above the surface to the top of the planetary boundary layer (PBL). However, it is assumed that they decrease exponentially with height from the PBL top upward. With this exponential decrease, when the altitude reaches the tropopause, background concentrations of aerosols acting as CCN reduce by a factor of ~10 as compared to those at the PBL top. The size distribution and composition of aerosols acting as CCN do not vary with height. Once background aerosol properties (i.e., aerosol number concentrations, size distribution and composition) are put into each grid point and time step, those properties at each grid point and time step do not change during the course of the simulations.

For the control-s and control-b runs, aerosol properties of INPs are not different from those of CCN except for the fact that the concentration of background aerosols acting as CCN is 100 times higher than the concentration of background aerosols acting as INPs at each time step and grid point, following a general difference between CCN and INPs in terms of their concentrations (Pruppacher and Klett, 1978).

Once clouds form and background aerosols start to be in clouds, those aerosols are not background aerosols anymore and the size distribution and concentrations of those aerosols begin to evolve through aerosol sinks and sources that include advection and aerosol activation (Fan et al., 2009). For example, once aerosols are activated, they are removed from the corresponding bins of the aerosol spectra. In clouds, after aerosol activation, aerosol mass starts to be inside hydrometeors and via collision-collection, it transfers to different types and sizes of hydrometeors. In the end, aerosol mass disappears in the atmosphere when hydrometeors with aerosol mass touches the surface. In non-cloudy areas, aerosol size and spatial distributions are designed to be identical to the size and spatial distributions of background aerosols, respectively. In other words, for this study, we use “the aerosol recovery method”. In this method, at any grid points, immediately after clouds disappear entirely, aerosol size distributions and number concentrations recover to background properties that background aerosols at those points have before those points are included in clouds. In this way, we can keep concentrations of background aerosols outside clouds in the simulations at observed counterparts. This enables spatiotemporal distributions of background aerosols in the simulations to mimic those distributions that

299 are observed and particularly associated with observed aerosol advection in reality. In the
300 aerosol recovery method, there is no time interval between the cloud disappearance and the
301 aerosol recovery. Here, when the sum of mass of all types of hydrometeors (i.e., water
302 drops, ice crystals, snow aggregates, graupel and hail) is not zero at a grid point, that grid
303 point is considered to be in clouds. When this sum becomes zero, clouds are considered to
304 disappear. Many studies using CSRM have employed this aerosol recovery method. They
305 have proven that with the recovery method, reasonable simulations of overall cloud and
306 precipitation properties are accomplished (e.g., Morrison and Grabowski, 2011; Lebo and
307 Morrison, 2014; Lee et al., 2016; Lee et al., 2018).
308
309 **3.3 Additional runs**
310
311 We repeat the control-s run by getting rid of aerosol-advection induced increases in
312 concentrations of aerosols acting as CCN as a way of investigating how the aerosol
313 advection affects the cloud system in the Seoul area. This repeated run is named the low-
314 aerosol-s run. An aerosol layer, which is advected from East Asia or from the west of the
315 Seoul area to it, increases aerosol concentrations in the Seoul area. There are stations in
316 islands in the Yellow Sea that monitor the aerosol advection (Eun et al., 2016; Ha et al.,
317 2019). To monitor and identify the aerosol advection, $PM_{2.5}$ which is measured by a station
318 in Baekryongdo island in Yellow Sea are compared to those which are measured in stations
319 in and around the Seoul area. In Figure 2a, a dot outside the inner rectangle marks the
320 island. The time evolution of $PM_{2.5}$ measured by the station on the island and the average
321 $PM_{2.5}$ over stations in the Seoul area, between 07:00 LST on December 22nd and 21:00 LST
322 on December 24th in 2017 when there is the strong advection of aerosols from East Asia to
323 the Seoul area, is shown in Figure 4. At 09:00 LST on December 22nd, the advection of
324 aerosols from East Asia enables aerosol mass to start going up and attain its peak around
325 05:00 LST on December 23rd on the island. Following this, aerosol mass starts to increase
326 in the Seoul area around 01:00 LST on December 23rd, and the mass attains its peak at
327 15:00 LST on December 23rd in the Seoul area. This is because aerosols, which are
328 advected from East Asia, move through the island to reach the Seoul area.

In the low-aerosol-s run, as a way of getting rid of aerosol-advection induced increases in concentrations of aerosols acting as CCN, it is assumed that $PM_{2.5}$, which is assumed to represent the mass of aerosols acting as CCN, and the associated background concentration of aerosols acting as CCN after 01:00 LST on December 23rd do not evolve with the aerosol advection in the Seoul area. Hence, the background concentration of aerosols acting as CCN is assumed to have that at 01:00 LST on December 23rd at each time step and grid point at the beginning of the simulation period. However, to isolate CCN effects on clouds, background aerosol concentration acting as INPs at each time step and grid point in the low-aerosol-s run is not different from that in the control-s run during the simulation period. In the observed PM data for the Seoul area, there is reduction in PM by a factor of ~10 on average over a period between ~07:00 and ~14:00 LST on December 24th, since precipitation scavenges aerosols (Figure 4). To emulate this scavenging and reflect it in background aerosols acting as CCN for the low-aerosol-s run, $PM_{2.5}$ and corresponding background concentrations of aerosols acting as CCN at each grid point is gradually reduced for the period between 07:00 and 14:00 LST on December 24th. This reduction is done in a way that background concentrations of aerosols acting as CCN at each grid point at 14:00 LST on December 24th is 10 times lower than that at 07:00 LST on December 24th in the low-aerosol-s run. Then, $PM_{2.5}$ and corresponding background concentrations of aerosols acting as CCN at each grid point at 14:00 LST on December 24th maintains until the end of the simulation period. This results in the evolution of the average $PM_{2.5}$ over the Seoul area in the low-aerosol-s run as shown in Figure 4. Here, the concentration of background aerosols acting as CCN, which is averaged over the whole domain and simulation period, in the control-s run is 3.1 times higher than that in the low-aerosol-s run. Via comparisons between the runs, how the increasing concentration of background aerosols acting as CCN due to the aerosol advection has an impact on clouds can be examined. The concentration of background aerosols acting as CCN is different among grid points and time steps in the control-s run. Hence, the ratio of the concentration of background aerosols acting as CCN between the runs is different among grid points and time steps.

For the Beijing case, to examine how aerosols acting as CCN affect clouds and precipitation, we repeat the control-b run with simply reduced concentrations of

background aerosols acting as CCN at each time step and grid point by a factor of 3.1. This repeated run is named the low-aerosol-b run. The 3.1-fold increase in aerosol concentrations from the low-aerosol-b run to the control-b is based on the 3.1-fold increase in the average concentration of background aerosols acting as CCN from the low-aerosol-s run to the control-s run. However, as in the control-s and low-aerosol-s runs, to isolate CCN effects on clouds, background aerosol concentration acting as INPs at each time step and grid point in the low-aerosol-b run is identical to that in the control-b run during the simulation period. Hence, on average, a pair of the control-s and low-aerosol-s runs has the same perturbation of aerosols acting as CCN as in a pair of the control-b and low-aerosol-b runs. Here, we define aerosol perturbation as a relative increase in aerosol concentration when compared to that before the increase occurs. The brief summary of all simulations in this study is given in Table 1.

4. Results

4.1 Cumulative precipitation

We compare the observed precipitation to the simulated counterpart in the control-s run for the Seoul case and in the control-b run for the Beijing case. For this comparison, the observed and simulated precipitation rates at the surface are averaged over the domain for each of the Seoul and Beijing cases (Figures 5a and 5b). Here, the simulated precipitation rates are smoothed over 1 hour. The comparison shows that the evolution of the simulated precipitation rate does not deviate from the observed counterpart significantly (Figures 5a and 5b).

In the Seoul case, overall, the precipitation rate is higher in the control-s run than in the low-aerosol-s run. As a result of this, the domain-averaged cumulative precipitation amount at the last time step is 14.1 mm and 12.0 mm in the control-s run and the low-aerosol-s run, respectively. The control-s run shows ~20 % higher cumulative precipitation amount. In the Beijing case, the evolution of the mean precipitation rate in the control-b run is not significantly different from that in the low-aerosol-b run. Due to this, the control-b run shows only ~2 % higher cumulative precipitation amount, despite the fact that the

concentrations of background aerosols acting as CCN are ~3 times higher in the control-b run than in the low-aerosol-b run. Note that in the Seoul case, the time- and domain-averaged concentration of background aerosols acting as CCN is also ~3 times higher in the control-s run than in the low-aerosol-s run. Despite this, the difference in the cumulative precipitation amount between the runs with different concentrations of background aerosols acting as CCN is greater in the Seoul case than in the Beijing case.

4.2 Precipitation, and associated latent-heat and dynamic processes

Figures 6a and 6b show the cumulative frequency distributions of precipitation rates at the last time step in the simulations for the Seoul and Beijing cases, respectively. In each of those figures, the observed frequency distribution is shown and compared to the simulated distribution. The observed distribution is obtained by interpolating and extrapolating the observed precipitation rates to grid points and time steps in each of the control-s and control-b runs. The observed maximum precipitation rates are 13.0 and 44.5 mm hr^{-1} for the Seoul and Beijing cases, respectively, and these maximum rates are similar to those in the control-s and control-b runs, respectively. Overall, the observed and simulated frequency distributions are in good agreement for each of the cases. This enables us to assume that results in the control-s (control-b) run are benchmark results to which results in the low-aerosol-s (low-aerosol-b) run can be compared to identify how aerosols acting as CCN have an impact on clouds and precipitation for the Seoul (Beijing) case. Here, it is notable that for the Beijing case, while differences in the cumulative precipitation amount between the control-b and low-aerosol-b runs are not significant, features in the frequency distribution of precipitation rates between those runs are substantially different (Figure 6b).

1) Seoul case

a. Precipitation Frequency distributions

Regarding precipitation whose rates are higher than ~2 mm hr^{-1}, the cumulative precipitation frequency at the last time step is higher in the control-s run as compared to

that in the low-aerosol-s run (Figure 6a). In particular, for the precipitation rate of 11.4 mm h^{-1}, there is an increase in the cumulative frequency by a factor of as much as ~10 in the control-s run. When it comes to precipitation rates above 11.5 mm hr^{-1}, precipitation is present in the control-s run and precipitation is absent in the low-aerosol-s run. Regarding precipitation whose rates are lower than ~2 mm hr^{-1}, differences in the cumulative frequency between the runs are insignificant. Hence, we see that there are significant increases in the frequency of relatively heavy precipitation whose rates are above ~2 mm hr^{-1} in the control-s run when compared to that in the low-aerosol-s run. At the last time step, this results in a larger amount of cumulative precipitation in the control-s run than in the low-aerosol-s run.

The time evolution of the cumulative precipitation frequency is shown in Figure 7. At 06:00 LST December 24th 2017, which corresponds to the initial stage of the precipitation development, the maximum precipitation rate reaches ~3 mm hr^{-1} and there is the greater frequency over most of precipitation rates in the control-s run than in the low-aerosol-s run (Figure 7a). With the time progress from 06:00 LST to 10:00 LST, the maximum precipitation rate increases to reach 12 mm hr^{-1} and the cumulative frequency is higher over precipitation whose rates are higher than ~3 mm hr^{-1} in the control-s run, while for precipitation whose rates are lower than ~3 mm hr^{-1}, differences in the cumulative frequency between the runs are negligible (Figures 7a and 7b). When time reaches 12:00 LST, which is around time when the peak in the evolution of the area-averaged precipitation rates occurs and thus the system is at its mature stage, the maximum precipitation rate increases up to ~13 mm hr^{-1} (Figures 5a and 7c). The basic patterns of differences in the cumulative precipitation frequency between the runs with the maximum precipitation rate around 13 mm hr^{-1}, which are established at 12:00 LST, maintain until the end of the simulation period (Figures 6a and 7c).

b. Condensation, deposition, updrafts and associated variables

Note that the source of precipitation is precipitable hydrometeors which are raindrops, snow, graupel and hail particles. Droplets and ice crystals are the source of those precipitable hydrometeors mostly via collision and coalescence processes. Droplets and ice

crystals gain their mass mostly via condensation and deposition. Based on this, to explain the greater cumulative precipitation amount in the control-s run than in the low-aerosol-s run, the evolutions of differences in condensation, deposition and associated updrafts between the runs are analyzed. The vertical profiles of differences in the area-averaged condensation, deposition and freezing rates, updraft mass fluxes and the associated mass density of each class of hydrometeors between the runs at 03:20, 03:40, 06:00 and 12:00 LST are shown in Figure 8. In Figure 8, differences in freezing rates are added for a more comprehensive understanding of processes that are related to differences in cumulative precipitation amount between the runs. Freezing includes riming processes between liquid and solid hydrometeors and these riming processes act as a source of precipitable hydrometeors. Cloud fractions are 0.32 (0.30), 0.85 (0.82), 0.93 (0.92) and 1.00 (1.00) in the control-s (low-aerosol-s) run at 03:20, 03:40, 06:00 and 12:00 LST, respectively. We see that cloud fraction does not vary significantly between the runs. Note that in all of figures, which display snow and hail mass density and include Figure 8, snow mass density includes ice-crystal mass density, while hail mass density includes graupel mass density for the sake of the display brevity. In Figure 8, horizontal black lines represent the altitudes of freezing and melting.

Condensation rates in the control-s run start to be larger than that in the low-aerosol-s run at 03:20 LST (Figure 8a). Higher aerosol or CCN concentrations induce more nucleation of droplets, higher cloud droplet number concentration (CDNC) and associated greater integrated surface of droplets in the control-s run. CDNC, which is averaged over grid points and time steps with non-zero CDNC, is 1050 and 352 cm^{-3} in the control-s and low-aerosol-s runs, respectively. Hence, more droplet surface is provided for water vapor to condense onto in the control-s run. This leads to more condensation in the control-s run. This establishes stronger feedbacks between updrafts and condensation, leading to greater droplet (or cloud-liquid) mass at 03:20 LST in the control-s run (Figure 8a). Then, these stronger feedbacks, which involve stronger updrafts particularly above 2 km in altitude, subsequently induce greater deposition and snow mass as time progresses from 03:20 LST to 03:40 LST, while more condensation and greater droplet mass maintain in the control-s run with the time progress to 03:40 LST (Figure 8b). These stronger updrafts enable clouds to grow higher in the control-s run. This eventually leads to a situation where the maximum

cloud depth is ~7 km in the control-s run and this depth is ~5 % deeper than that in the low-aerosol-s run for the whole simulation period.

Through aerosol-induced stronger feedbacks between condensation, deposition and updrafts in the control-s run, while more condensation and more overall deposition maintain in the control-s run, differences in condensation and deposition between the control-s and low-aerosol-s runs increase as time progresses from 03:40 LST to 06:00 LST (Figures 8b and 8c). Associated with this, the greater mass of raindrops and hail particles appears up, while the greater mass of droplets and snow in the control-s run than in the low-aerosol-s run maintains with the time progress from 03:40 LST to 06:00 LST (Figure 8c). At 06:00 LST, there is more freezing starting to occur in the control-s run than in the low-aerosol-s run. However, differences in freezing are ~one and ~two orders of magnitude smaller than those in deposition and condensation, respectively. After 06:00 LST until time reaches 12:00 LST when the overall differences in the cumulative precipitation frequency between the runs are established, differences in freezing become at an order of magnitude, which is similar to that of differences in deposition, and become around one order of magnitude smaller than those in condensation (Figures 8c and 8d). The greater mass of hydrometeors in the control-s run also continues after 06:00 LST until time reaches 12:00 LST (Figures 8c and 8d). At 12:00 LST, condensation, deposition and freezing rates are still higher in the control-s run. Here, we see that CCN-induced more cumulative precipitation amount and associated differences in the precipitation frequency distribution between the control-s and low-aerosol-s runs are primarily associated with CCN-induced more condensation which induce CCN-induced more deposition and higher mass density of hydrometeors as sources of precipitation but weakly connected to CCN-induced changes in freezing. This is supported by the fact that the time- and domain-averaged differences in freezing rate are ~one to ~two order of magnitude smaller than those in condensation and deposition rates.

c. Condensation frequency distributions and horizontal distributions of condensation and precipitation

Based on the importance of condensation for CCN-induced changes in precipitation, the horizontal distribution of the column-averaged condensation rates over the domain and the cumulative frequency distribution of the column-averaged condensation rates at each time step is obtained. To better visualize the role of condensation in precipitation, the horizontal distribution of the column-averaged condensation rates is superimposed on that of precipitation rates (Figure 9). At 03:40 LST, condensation mainly occurs around the northern part of the domain as marked by a yellow rectangle. The synoptic wind condition in the marked area favors the collision between northward and southward wind and the associated convergence around the surface (Figures 9a and 9b). This convergence induces updrafts and condensation in the marked area. In the marked area, more aerosols acting as CCN induce more and more extensive condensation, which leads to the higher domain-averaged condensation rates in the control-s run than in the low-aerosol-s run (Figures 8b, 9a and 9b). More droplets are formed on more aerosols acting as CCN and more droplets provide more surface areas where condensation occurs and this enables more and more extensive condensation in the control-s run than in the low-aerosol-s run (Figures 8b, 9a and 9b). At 06:20 LST, a precipitating system is advected into the domain via the western boundary, and as seen in Figures 9c and 9d for 07:20 LST, as time progresses to 07:20 LST, the advected precipitating system is further advected to the east and extended mostly over areas in the northern part of the domain where condensation mainly occurs. This confirms that condensation is the main source of cloud mass and precipitation. In the eastern part of the domain, there are mountains and in particular, higher mountains are on the northeastern part of the domain than in the other parts of the domain. These higher mountains induce forced convection and associated condensation more effectively in the northeastern part than in the other parts. This is in favor of the precipitating system that extends further to the east in the northern part of the domain. Due to more aerosols acting as CCN, condensation, which is induced by forced convection over mountains, is more and more extensive in the control-s run (Figures 9c and 9d).

As time progresses to 08:40 LST, the precipitating system moves eastward further in the northern part of the domain and the system in the control-s run extends to the east further as compared to that in the low-aerosol-s run (Figures 9e and 9f). In association with more aerosols acting as CCN and associated more condensation over mountains in the

northeastern part, there is more extension of the system in the control-s run than in the low-aerosol-s run. This enables the system in the control-s run to reach the eastern boundary at 08:40 LST, which is earlier than in the low-aerosol-s run (Figures 9e and 9f). The system in the low-aerosol-s run reaches the eastern boundary at 09:00 LST. Here, we see that although aerosols acting as CCN do not change overall locations of the precipitation system, they affect how fast the system extends to the east by affecting the amount of condensation which is produced by forced convection. Associated with this, as seen in Figure 10, the control-s run has the much higher cumulative condensation frequency than the low-aerosol-s run over all of condensation rates during the period between 07:20 and 09:00 LST. Contributed by this, the higher precipitation frequency over most of precipitation rates occurs in the control-s run during and after the period (Supplementary Figures 1a and 1b and Figures 7b and 7c).

At 10:00 LST, in the southern part of the domain, there is a precipitating area forming as marked by a yellow rectangle (Figures 9g and 9h). The precipitation area in the southern part of the domain extends and merge into the advecting main precipitating system in the northern part of the domain as time progresses to 11:00 LST (Figures 9i and 9j). The merge leads to precipitation that occupies most of the domain at 12:00 LST (Figures 9k and 9l). After 10:00 LST, associated with this merge, the maximum precipitation rate increases to 13 mm hr^{-1} at 12:00 LST (Figures 7c). After 13:00 LST, the precipitation enters its dissipating stage and its area reduces and nearly disappears. Even after the merge, CCN-induced more condensation maintains and this in turn contributes to a situation where the control-s run has the greater precipitation frequency over most of precipitation rates than in the low-aerosol-s run until the simulations progress to their last time step (Figures 6a, 7c and 8d).

2) Beijing case

Stronger convection and deeper clouds develop in the Beijing case than in the Seoul case. The maximum cloud depth is ~7 and ~12 km in the control-s and control-b runs, respectively. In the Seoul case, clouds do not reach the tropopause, while they reach the tropopause in the Beijing case. Deeper clouds in the Beijing case produce the maximum

precipitation rate of ~45 mm hr^{-1} in the control-b run. However, less deep clouds in the Seoul case produce the maximum precipitation rate of ~13 mm hr^{-1} in the control-s run (Figure 6).

a. Precipitation frequency distributions

When it comes to precipitation whose rates are higher than ~12 mm hr^{-1}, the control-b run has the higher cumulative precipitation frequency at the last time step than the low-aerosol-b run (Figure 6b). Particularly, for the precipitation rates of 28.1 and 30.0 mm hr^{-1}, the cumulative frequency increases by a factor of as much as ~10. Moreover, regarding precipitation rates higher than ~33 mm hr^{-1}, precipitation is present in the control-b run, however, precipitation is absent in the low-aerosol-b run. Hence, we see that the frequency of comparatively heavy precipitation whose rates are higher than ~12 mm hr^{-1} rises significantly in the control-b run as compared to that in the low-aerosol-b run. Below ~2 mm hr^{-1}, there is also the greater precipitation frequency in the control-b run than in the low-aerosol-b run. Unlike the situation for precipitation rates above ~12 mm hr^{-1} and below ~2 mm hr^{-1}, for precipitation rates from ~2 mm hr^{-1} to ~12 mm hr^{-1}, the control-aerosol-b run has the lower precipitation frequency than in the low-aerosol-b run. Here, we see that the higher precipitation frequency above ~12 mm hr^{-1} and below ~2 mm hr^{-1} balances out the lower precipitation frequency between ~2 and ~12 mm hr^{-1} in the control-b run. This results in the similar cumulative precipitation amount between the runs.

Figure 11 shows the time evolution of the cumulative precipitation frequency. When precipitation starts around 16:00 LST, the higher precipitation frequency occurs over most of precipitation rates in the low-aerosol-run-b run than in the control-b run (Figure 11a). At 16:00 LST, the maximum precipitation rate is lower than 1.0 mm hr^{-1} for both of the runs. As time progresses to 17:00 LST, the maximum precipitation rate increases to ~17 mm hr^{-1} and the higher (lower) cumulative precipitation frequency over precipitation rates higher than ~12 mm hr^{-1} (between ~2 and ~12 mm hr^{-1}) in the control-b run than in the low-aerosol-b run, which is described above as shown in Figure 6b for the last time step, starts to emerge (Figure 11b). At 17:20 LST, the higher frequency for precipitation rates below 2 mm hr^{-1} in the control-b run, which is also described above as shown in Figure 6b

for the last time step, starts to show up, while the higher (lower) frequency for precipitation rates higher than ~12 mm hr^{-1} (between ~2 and ~12 mm hr^{-1}) in the control-b run, which is established at 17:00 LST, maintains as time progresses from 17:00 LST to 17:20 LST (Figure 11c). At 17:20 LST, the maximum precipitation rate increases to 42 (19) mm hr^{-1} in the control-b (low-aerosol-b) run (Figure 11c). At 19:00 LST, the maximum precipitation rate increases to ~45 (33) mm hr^{-1} for the control-b (low-aerosol-b) run, while the qualitative nature of differences in the precipitation frequency distributions with the tipping precipitation rates of ~2 and ~12 mm hr^{-1} between the runs does not vary much between 17:20 and 19:00 LST (Figures 11c and 11d). The qualitative nature of differences in the cumulative precipitation frequency between the runs and the maximum precipitation rates in each of the runs, which are established at 19:00 LST, do not vary significantly until the end of the simulation period (Figures 6b and 11d).

b. Condensation, deposition, updrafts and associated variables

As done for the Seoul case, as a way of better understanding differences in the cumulative precipitation amount and frequency between the control-b and low-aerosol-b runs, the evolutions of differences in the vertical distributions of the area-averaged condensation rates, deposition rates, freezing rates, the mass density of each class of hydrometeors and updrafts mass fluxes are obtained and shown in Figures 12. Cloud fractions are 0.12 (0.11), 0.25 (0.22), 0.36 (0.32), 0.43 (0.40) and 0.48 (0.47) in the control-b (low-aerosol-b) run at 14:20, 15:40, 16:00, 17:20 and 19:00 LST, respectively. Here, we see that cloud fraction does not vary significantly between the runs. In Figure 12, horizontal black lines represent the altitudes of freezing and melting. As seen in Figure 5b, precipitation starts around 16:00 LST but differences in condensation rates start at 14:20 LST with higher condensation rates in the control-b run (Figure 12a). Similar to the situation in the Seoul case, higher concentrations of aerosols acting as CCN induce more nucleation of droplets, higher CDNC and associated greater integrated surface of droplets in the control-b run. CDNC, which is averaged over grid points and time steps with non-zero CDNC, is 992 and 341 cm^{-3} in the control-b and low-aerosol-b runs, respectively. Hence, more droplet surface is provided for water vapor to condense onto in the control-b run. This leads to more

638 condensation in the control-b run. Due to this, cloud-liquid or droplet mass becomes greater
639 in the control-b run at 14:20 LST (Figure 12a). Increased condensation rates induce
640 increased condensational heating and thus intensified updrafts (Figure 12a). These
641 updrafts enable the maximum cloud depth to be ~ 12 km in the control-b run and this depth
642 is just ~1 % deeper than that in the low-aerosol-b run for the whole simulation period. This
643 negligible difference in the maximum cloud depth between the runs is due to the fact that
644 clouds with the maximum depth reach the tropopause in both of runs and thus there is not
645 much wiggle room to make significant differences in cloud depth between the runs.
646 When time reaches 15:40 LST, deposition rates and snow mass start to show
647 differences between the runs, while higher condensation rates and droplet mass maintain
648 in the control-b run with the time progress from 14:20 LST to 15:40 LST. However, unlike
649 the situation in the Seoul case, higher concentrations of aerosols acting as CCN result in
650 lower deposition rates and snow mass in the control-b run (Figure 12b). When time
651 progresses from 15:40 LST to 16:00 LST, differences in freezing start to occur and freezing
652 rates are lower (higher) at altitudes between ~6 and ~8 km (~4 and ~6 km), while higher
653 condensation rates and droplet mass, and lower snow mass maintain in the control-b run
654 (Figure 12c). Due to stronger updrafts, which are mainly ascribed to more condensation,
655 deposition rates start to be higher at altitudes between ~7 and ~9 km and freezing rates are
656 higher at altitudes between ~4 and ~6 km in the control-b run with the time progress from
657 15:40 LST to 16:00 LST (Figure 12c). Differences in freezing rates are at the same order
658 of magnitude of those in deposition and ~two orders of magnitude smaller than those in
659 condensation at 16:00 LST (Figure 12c). At 16:00 LST, differences in hail mass between
660 the runs appear up and hail mass is slightly lower in the control-b run (Figure 12c). At
661 17:20 LST, overall, freezing rates are lower at altitudes between ~4 and ~8 km, while
662 overall, snow and hail mass is still lower, and droplet mass is still higher in the control-b
663 run (Figure 12d). Differences in freezing rates are at the same order of magnitude of those
664 in deposition and ~one orders of magnitude smaller than those in condensation at 17:20
665 LST (Figure 12d). Due to more condensation and droplet mass, greater raindrop mass
666 appears up in the control-b run at 17:20 LST (Figure 12d). As the time progresses to 19:00
667 LST, deposition rates become lower at the altitudes from ~7 km to ~12 km and overall
668 freezing rates become higher at altitudes from ~ 4 km to ~10 km in the control-b run (Figure

12e). Overall, lower snow and hail mass maintains in the control-b run as time progresses from 17:20 LST to 19:00 LST. As time progresses from 17:20 LST to 19:00 LST, overall higher condensation rates, droplet and raindrop mass maintain in the control-b run (Figure 12e). Here, while the time- and domain-averaged deposition (condensation and freezing) rates are lower (higher) in the control-b run over the whole simulation period, the average differences in freezing rates are ~one to ~two orders of magnitude smaller than those in deposition and condensation rates between the runs. Hence, more condensation (but not deposition and freezing) is a main cause of stronger updrafts in the control-b run. More condensation and more freezing tend to induce increases in the mass of precipitable hydrometeors in the control-b run. Less deposition tends to induce decreases in the mass of precipitable hydrometeors in the control-b run. This competition between condensation, deposition and freezing leads to negligible differences in the cumulative precipitation amount at the last time step between the control-b and low-aerosol-b runs, although roles of freezing in this competition are negligible as compared to those of condensation and deposition.

c. Condensation frequency distributions, horizontal distributions of condensation and precipitation, and condensation-precipitation correlations

Figure 13 shows the horizontal distribution of the column-averaged condensation rates over the domain and Figure 14 shows the cumulative frequency distributions of column-averaged condensation rates at selected times. As in the Seoul case, the horizontal distribution of condensation rates is superimposed on that of precipitation rates and the terrain in Figure 13. At 14:20 LST, condensation starts to occur in places with mountains, which induce forced convection, and condensation is concentrated around the center of the domain as marked by a yellow circle (Figures 13a and 13b). Note that condensation does not occur in the plain area which is the south of the 100-m terrain-height contour line (Figures 13a and 13b). Due to higher concentrations of aerosols acting as CCN, there is more condensation around the center in the control-b run than in the low-aerosol-b run (Figures 13a and 13b). This leads to a situation where the control-b run has the higher area-

700 averaged condensation rates than the low-aerosol-b run (Figure 12a). Then, as time
701 progresses to 17:20 LST, the condensation area extends to the eastern and western parts of
702 the domain mostly over mountain areas (Figures 13c and 13d). Hence, the main source of
703 condensation is considered to be forced convection over mountains. As seen in Figures 13c
704 and 13d, higher concentrations of aerosols acting as CCN induce the control-b run to have
705 much more condensation spots and thus much bigger areas with condensation than the low-
706 aerosol-b run at 17:20 LST. Associated with this, CCN-induced more condensation in the
707 control-b run maintains with the time progress to 17:20 LST (Figure 12d). At 17:20 LST,
708 precipitation mainly occurs in a spot which is in the western part of areas with relatively
709 high condensation rates (Figures 13c and 13d).
710 At 17:20 LST, as seen in the cumulative frequency of condensation rates, the control-
711 b run has the higher condensation frequency above condensation rate of ~10 $\times 10^{-3}$ g m^{-3} s^{-1}
712 and below that of ~3$\times 10^{-3}$ g m^{-3} s^{-1} than the low-aerosol-b run (Figure 14a). This pattern
713 of differences in the condensation frequency distribution with the tipping condensation-
714 rate points at ~10 $\times 10^{-3}$ and ~3 $\times 10^{-3}$ g m^{-2} s^{-1} continues up to 19:00 LST (Figures 14b).
715 Figure 15 shows the mean precipitation rate over each of the column-averaged
716 condensation rates for the period up to 17:20 LST in the control-b run. A column-averaged
717 condensation rate in an air column with a precipitation rate at its surface is obtained and
718 these condensation and precipitation rates are paired at each column and time step. Then,
719 collected precipitation rates are classified and grouped based on the corresponding paired
720 column-averaged condensation rates. The classified precipitation rates corresponding to
721 each of the column-averaged condensation rates are averaged arithmetically to construct
722 Figure 15. There are only less than 10 % differences in the mean precipitation rate for each
723 of the column-averaged condensation rates between the control-b and low-aerosol-b runs
724 (not shown). Figure 15 shows that generally a higher condensation rate is related to a higher
725 mean precipitation rate. It is also roughly shown that, according to the mean precipitation
726 rate for each condensation rate, overall, condensation rates below ~3 $\times$ 10^{-3} g m^{-3} s^{-1} and
727 above ~10 $\times$ 10^{-3} g m^{-3} s^{-1} are correlated with precipitation rates below ~2 mm hr^{-1} and
728 above ~12 mm hr^{-1}, respectively, while condensation rates between ~3 and ~10 $\times$ 10^{-3} g
729 m^{-3} s^{-1} are correlated with precipitation rates between ~2 and ~12 mm hr^{-1} (Figure 15).
730 Hence, on average, the higher frequency of condensation with rates above ~10 $\times$ 10^{-3} g m^{-}

731 ^{3} s^{-1} and below ~ 3 × 10^{-3} g m^{-3} s^{-1} can be considered to lead to the higher frequency of
732 precipitation whose rates are higher than ~12 mm hr^{-1} and lower than ~ 2 mm hr^{-1} in the
733 control-b run, respectively. It can also be considered that the lower condensation frequency
734 between ~3 and ~10 × 10^{-3} g m^{-3} s^{-1} leads to the lower precipitation frequency between ~2
735 and ~12 mm hr^{-1} in the control-b run. It is found that this correspondence between
736 condensation and precipitation rates is valid whether analyses to construct Figure 15 are
737 repeated only for a time point at 16:30 LST or for a period between 16:30 and 17:00 LST.
738 These time point and period are related to analyses of the moist static energy as described
739 in Section e below.
740 At 17:20 LST, the larger precipitation frequency between ~2 and ~12 mm hr^{-1} in the
741 low-aerosol-b run nearly offsets the larger precipitation frequency in the other ranges of
742 precipitation rates in the control-b run (Figure 11c). This leads to the similar average
743 precipitation rate between the runs at 17:20 LST and contributes to the similar cumulative
744 precipitation at the last time step between the runs (Figure 5b).
745
746 **d. Evaporation and gust fronts**
747
748 As time progresses from 17:00 to 19:00 LST, the precipitation system moves northward
749 (Figure 16). At the core of the precipitation system, due to evaporation and downdrafts,
750 there is the horizontal outflow forming at 17:00 LST (Figures 16a and 16b). The core is
751 represented by the field of precipitation whose rates are higher than 1 mm hr^{-1} in Figure 16.
752 At the core, the northward outflow is magnified by the northward synoptic-scale wind,
753 while at the core, the outflow in the other directions is offset by the northward synoptic-
754 scale wind. Hence, the outflow is mainly northward from 17:00 LST onwards as marked
755 by yellow circles in Figures 16. This enables convergence or a gust front, which is produced
756 by the outflow from the core, to be mainly formed at the north of the core. Note that the
757 intensity of a gust front is proportional to that of outflow from a core of precipitation or
758 convective system (Weisman and Klemp, 1982; Houze, 1993). The strong gust front at the
759 north of the core generates strong updrafts, a significant amount of condensation and
760 precipitation. Then, a subsequent area with clouds and precipitation is formed at the north
761 of the core as time progresses, which means that the precipitation system extends or moves

762 to the north as seen in comparisons between sub-panels with different times in Figure 16.
763 This movement, which is induced by collaborative work between outflow, synoptic wind
764 and gust fronts, is typical in deep convective clouds.

765 As described above, the more droplet nucleation and greater integrated droplet surface
766 induce more condensation before 17:00 LST in the control-b run. This and lower efficiency
767 of collision and collection among droplets enable the control-b run to have a larger amount
768 of cloud liquid or droplets as a source of evaporation. This in turn enables more droplet
769 evaporation, more associated cooling and stronger downdrafts, although less rain
770 evaporation is in the control-b run particularly for the period from 17:00 LST to 19:00 LST
771 (Figure 17). More evaporation of droplets and associated stronger downdrafts with higher
772 concentrations of aerosols acting as CCN have been shown by the numerous previous
773 studies (e.g., Tao et al., 2007; Tao et al., 2012; Khain et al., 2008; Lee et al., 2018).

774 During the period between 17:00 and 19:00 LST, with the development of convergence
775 or the gust front, as mentioned above, the maximum precipitation rate increases from ~ 17
776 (17) to ~ 45 (33) mm hr^{-1} in the control-b (low-aerosol-b) run (Figure 11). This indicates
777 that the gust-front development contributes to the overall intensification of the precipitation
778 system, while it moves northward. If there were only northward synoptic-scale wind with
779 no formation of the gust front, the system would move northward with less intensification.
780 Over the period from 17:00 LST to 19:00 LST, stronger downdrafts and associated stronger
781 outflow generate a stronger gust front and more subsequent condensation in the control-b
782 run. This enhances the small initial difference, which is at 17:00 LST, in the frequency of
783 precipitation with rates above ~12 mm hr^{-1} between the runs substantially as time
784 progresses from 17:00 LST to 19:00 LST (Figure 11). Associated with this, with the time
785 progress, the nearly identical maximum precipitation rate between the runs at 17:00 LST
786 turns into the significantly higher maximum precipitation rate in the control-b run than in
787 the low-aerosol-b run (Figure 11). Around 19:00 LST, the system enters its dissipating
788 stage, accompanying reduction in the precipitating area and the area-averaged precipitation
789 rate (Figures 5b, 16m and 16n).
790
791 **e. Moist static energy**
792

Condensation, which controls droplet mass and precipitation, is controlled by updrafts and updrafts are in turn controlled by instability. One of important factors that maintain instability is the moist static energy. Motivated by this, to better understand differences in the precipitation frequency distribution in association with those in the condensation frequency distribution between the control-b and low-aerosol-b runs, we calculate the flux of the moist static energy and the flux is defined as follows:

$$\overrightarrow{Fs} = S \times \rho \times \vec{V} \qquad (1),$$

where $\overrightarrow{Fs}$ represents the flux of the moist static energy, S the moist static energy, ρ the air density and $\vec{V}$ the horizontal-wind vector. In Eq. (1), we see that the flux is in the vector form and has two components, which are its magnitude and direction. The fluxes of the moist static energy in the PBL are obtained over the domain at 16:30 LST, since in general, the moist static energy in the PBL has much stronger effects on instability and updrafts than that above the PBL. In particular, we focus on the PBL fluxes of the energy that cross the boundary over a time step at 16:30 LST between areas with the column-averaged condensation rate from 3×10^{-3} g m^{-3} s^{-1} to 10×10^{-3} g m^{-3} s^{-1}, which are referred to as "area A", and those with the column-averaged condensation rate above 10×10^{-3} g m^{-3} s^{-1}, which are referred to as "area B". This is because we are interested in the exchange of the moist static energy between areas A and B and this exchange can be seen by looking at those fluxes which cross the boundary between those areas.

We are interested in the exchange of the energy, since we hypothesized that the exchange somehow alters instability in each of areas A and B in a way that there are increases (decreases) in instability, the updraft intensity, condensation and precipitation with increasing concentrations of aerosols acting as CCN in area B (A), leading to the higher (lower) frequency of condensation whose rates are higher than 10×10^{-3} g m^{-3} s^{-1} (between 3×10^{-3} and 10×10^{-3} g m^{-3} s^{-1}) and precipitation whose rates are higher than 12 mm hr^{-1} (between 2 and 12 mm hr^{-1}) in the control-b run than in the low-aerosol-b run. When the PBL fluxes, which crosses the boundary over the time step at 16:30 LST, are summed at 16:30 LST, there is the net flux from area A to area B. This means that there is the net transportation of the moist static energy from areas with condensation rates between

824 3×10^{-3} and 10×10^{-3} g m^{-3} s^{-1} to those with condensation rates greater than 10×10^{-3} g m^{-3}
825 s^{-1} in the PBL at 16:30 LST as shown in Table 2. Table 2 shows the net summed flux of the
826 moist static energy which crosses the boundary between areas A and B in the control-b run
827 as well as the low-aerosol-b run. To calculate the net flux at 16:30 LST in Table 2, the
828 fluxes, which cross the boundary between areas A and B over the time step at 16:30 LST,
829 only at grid points in the PBL are summed. For the calculation, the flux from area A to area
830 B has a positive sign, while the flux from area B to area A has a negative sign. Since the
831 net flux is positive for both of the runs as shown in Table 2, there is the net flux from area
832 A to area B in the PBL. The above-described analysis for the fluxes crossing the boundary
833 between areas A and B is repeated for every time step between 16:30 and 17:00 LST and
834 based on this, the net summed flux over the period between 16:30 and 17:00 LST is
835 obtained. As shown in Table 2, the net flux for the period between 16:30 and 17:00 LST is
836 also positive as in the situation only for 16:30 LST. This means that there is the net
837 transportation of the moist static energy from area A to area B in the PBL during the period
838 between 16:30 and 17:00 LST.

839 At 16:30 LST, condensation with rates above 10×10^{-3} g m^{-3} s^{-1} starts to develop and
840 this forms area B. Area B has stronger updrafts via greater condensational heating than in
841 other areas, including area A, with lower condensation rates. Stronger updrafts in area B
842 induce the convergence of air and associated moist static energy from area A to area B.
843 Since the average condensation rate and updrafts at 16:30 LST over area B are higher and
844 stronger due to increasing concentrations of aerosols acting as CCN, respectively, the air
845 convergence and the associated transportation of the moist static energy in the PBL from
846 area A to area B are stronger and more, respectively, in the control-b run than in the low-
847 aerosol-b run (Table 2). Stated differently, area B steals the moist static energy from area
848 A, and this occurs more effectively in the control-b run. This increases instability and
849 further intensifies updrafts in area B, and decreases instability and weakens updrafts in area
850 A, while these increases and decreases (intensification and weakening) of instability
851 (updrafts) are greater in the control-b run for the period from 16:30 LST to 17:00 LST.
852 This increases condensation, cloud mass and precipitation whose rates are higher than 12
853 mm hr^{-1} in area B, and decreases condensation, cloud mass and precipitation whose rates
854 are from 2 mm hr^{-1} to 12 mm hr^{-1} in area A. These increases and decreases occur more

855 effectively for the control-b run than for the low-aerosol-b run during the period. This in
856 turn leads to the lower precipitation frequency for the precipitation rates from 2 mm hr^{-1} to
857 12 mm hr^{-1} and the higher frequency for the precipitation whose rates are higher than 12
858 mm hr^{-1} at 17:00 LST in the control-b run (Figure 11b). The weakened updrafts and reduced
859 condensation turn a portion of precipitation with rates between 2 and 12 mm hr^{-1} to
860 precipitation whose rates are below 2 mm hr^{-1}, and this takes place more efficiently in the
861 control-b run during the period between 16:30 and 17:00 LST. This eventually increases
862 the frequency of precipitation rates below 2 mm hr^{-1} and this increase is greater for the
863 control-b run, leading to the greater precipitation frequency for the precipitation rates
864 below 2 mm hr^{-1} in the control-b run at 17:20 LST (Figure 11c).
865
866 ## 5. Discussion
867
868 ### 5.1 Comparison of the Seoul and Beijing cases
869
870 In this section, we compare the Seoul case to the Beijing case. For the comparison,
871 remember that on average, a pair of the control-s and low-aerosol-s runs has the same
872 perturbation of aerosols acting as CCN as in a pair of the control-b and low-aerosol-b runs.
873 Associated with the fact that clouds in the Seoul case are less deep than those in the Beijing
874 case, overall, updrafts in the Seoul case are not as strong as those in the Beijing case. Hence,
875 unlike the situation in the Beijing case, stronger updrafts, which accompany higher
876 condensation rates, and associated convergence in the Seoul case are not strong enough to
877 steal the sufficient amount of the moist static energy from weaker updrafts which
878 accompany lower condensation rates. This makes the redistribution of the moist static
879 energy between areas with relatively higher condensation rates and those with relative
880 lower condensation rates, such as that between areas A and B for the Beijing case,
881 ineffective for the Seoul case. Due to this, the sign of CCN-induced changes in the
882 frequency of precipitation rates does not vary throughout all of the precipitation rates
883 except for the range of low precipitation rates where there are nearly no CCN-induced
884 changes in the frequency in the Seoul case as shown in Figure 6a. As seen in Figure 6a,
885 mainly due to increases in condensation and deposition, precipitation frequency increases

for most of precipitation rates, although the precipitation frequency does not show significant changes as concentration of aerosols acting as CCN increases for relatively low precipitation rates in the control-s run as compared to that in the low-aerosol-s run. This means that there are no tipping precipitation rates where the sign of CCN-induced changes in the frequency of precipitation rates changes in the Seoul case, contributing to the higher cumulative precipitation amount in the simulation with higher concentrations of aerosols acting as CCN for the Seoul case, which are different from the situation in the Beijing case.

In the Beijing case with deeper clouds as compared to those in the Seoul case, clouds develop gust fronts via strong downdrafts and associated strong outflow. These gust fronts play an important role in developing strong convection and associated high precipitation rates. Unlike the situation in the Seoul case, there are strong clouds and associated updraft entities that are able to steal heat and moisture (or the moist static energy) as sources of instability from areas with relatively less strong clouds and updrafts with medium strength; note that these strong clouds here involve stronger updrafts via greater condensational heating as described in Section e above and this enables these clouds to be thicker and have higher cloud mass than these less strong clouds. This further intensifies strong clouds and weakens less strong clouds with medium strength. Due to this, the cumulative frequency of heavy (medium) precipitation in association with strong clouds (less strong clouds with medium strength) increases (decreases). Some of the weakened clouds eventually produce light precipitation, which increase the cumulative frequency for light precipitation. The intensification of strong clouds and the weakening of less strong clouds with medium strength gets more effective with increasing concentration of aerosols acting as CCN. Hence, in the Beijing case, for medium precipitation in association with less strong clouds, the simulation with higher concentration of aerosols acting as CCN shows the lower cumulative precipitation frequency at the last time step. However, for heavy precipitation, which is associated with strong clouds, and light precipitation, the simulation with higher concentrations of aerosols acting as CCN shows the higher cumulative precipitation frequency at the last time step. These differential responses of precipitation to increasing concentration of aerosols acting as CCN among different types of precipitation occur in the circumstances of the similar cumulative precipitation amount between the simulations with different concentration of aerosols acting as CCN. This similar precipitation amount is due

to above-mentioned competition between CCN-induced changes in condensation, deposition and freezing.

In both of the Seoul and Beijing cases, CCN-induced changes in condensation plays an important role in making differences in the precipitation amount and/or the precipitation frequency distribution between the simulations with different concentration of aerosols acting as CCN. It is notable that in less deep clouds in the Seoul case, in addition to condensation, deposition plays a role in precipitation to induce CCN-induced increases in the precipitation amount. CCN-induced increases in condensation initiate the differences in cloud mass and precipitation and then CCN-induced increases in deposition follow to further enhance those differences. In deep clouds in the Beijing case, condensation tends to induce increases in cloud mass and precipitation, while deposition tends to induce decreases in cloud mass and precipitation with increasing concentration of aerosols acting as CCN. Hence, as clouds get shallower and thus ice processes become less active, the role of deposition in CCN-induced changes in precipitation amount turns from CCN-induced suppression of precipitation to enhancement of precipitation. Here, we find that contrary to the traditional understanding, the role of variation of freezing, which is induced by the varying concentration of aerosols acting as CCN but not INPs, in precipitation is negligible as compared to that of condensation and deposition in both of the cases.

6. Summary and conclusions

This study examines impacts of aerosols, which act as CCN, on clouds and precipitation in two metropolitan areas, which are the Seoul and Beijing areas, in East Asia that has experienced substantial increases in aerosol concentrations over the last decades. The examination is performed via simulations, which use a CSRM. These simulations are for deep clouds which reach the tropopause in the Beijing case and for comparatively less deep clouds which do not reach the tropopause yet grow above the level of freezing in the Seoul case.

In both of the cases, CCN-induced changes in condensation plays a critical role in CCN-induced variation of precipitation properties (e.g., the precipitation amount and the precipitation frequency distribution). In the Seoul case, CCN-induced increases in

condensation and subsequent increases in deposition lead to CCN-induced increases in the precipitation frequency over most of precipitation rates and thus in the precipitation amount. However, in the Beijing case, while there are increases in condensation with increasing CCN concentrations, there are decreases in deposition with increasing CCN concentrations. This competition between increases in condensation and decreases in deposition leads to negligible CCN-induced changes in cumulative precipitation amount in the Beijing case. In both of the cases, CCN-induced changes in freezing are negligible as compared to those in condensation and deposition. In the Beijing case, there is another competition for the moist static energy among clouds with different updrafts and condensation. This competition results in CCN-induced differential changes in the precipitation frequency distributions. With clouds getting deeper from the Seoul case to the Beijing case, clouds and associated updrafts, which are strong enough to steal the moist static energy from other clouds and their updrafts, appear. This makes strong clouds stronger and clouds with medium strength weaker. With higher CCN concentrations, strong clouds steal more energy, and thus strong clouds become stronger and clouds with medium strength weaker with a greater magnitude. As a result of this, there are more frequent heavy precipitation (whose rates are higher than 12 mm hr^{-1}) and light precipitation (whose rates are lower than 2 mm hr^{-1}), and less frequent medium precipitation (with rates from 2 mm hr^{-1} to 12 mm hr^{-1}) with increasing CCN concentrations in the Beijing case.

In both of the Seoul and Beijing cases, there are mountains and they play an important role in how cloud and precipitation evolve with time and space. In both of the cases, the precipitating system moves or expands over mountains which induce forced convection and generate condensation. This important role of mountains and forced convection in the formation and evolution of the precipitation system has not been examined much in the previous studies of aerosol-cloud interactions, since many of those previous studies (e.g., Jiang et al., 2006; Khain et al., 2008; Li et al., 2011; Morrison et al., 2011) have dealt with convective clouds that develop over plains and oceans. Hence, findings in this study, which are related to mountain-forced convection and its interactions with aerosols, can be complementary to those previous studies. Stated differently, this study can shed light on our path to the understanding of aerosol-cloud interactions over more general domains not only with no terrain but also with terrain.

Code/Data availability

Our private computer system stores the code/data which are private and used in this study. Upon approval from funding sources, the data will be opened to the public. Projects related to this paper have not been finished, thus, the sources prevent the data from being open to the public currently. However, if information on the data is needed, contact the corresponding author Seoung Soo Lee (slee1247@umd.edu).

Author contributions

Essential initiative ideas are provided by SSL, KJH and KHS to start this work. Simulation and observation data are analyzed by SSL, JC and GK. JU and YZ review the results and contribut to their improvement. CHJ and JG perform additional simulations, which are required by the review process, and their basic analyses. CHJ also provide ideas to handle the reviewers' comments.

Competing interests

The authors declare that they have no conflict of interest.

Acknowledgements

This study is supported by the National Research Foundation of Korea (NRF) grant funded by the Korea government (MSIT) (No. NRF2020R1A2C1003215) and the "Construction of Ocean Research Stations and their Application Studies" project funded by the Ministry of Oceans and Fisheries, South Korea. This study is also supported by the National Research Foundation of Korea (NRF) by FRIEND (Fine Particle Research Initiative in East Asia Considering National Differences) project through the National Research Foundation of Korea (NRF) funded by the Ministry of Science and ICT (2020M3G1A1114617). Authors thank Danhong Dong at Chinese Academy of Sciences and Fang Wu at Beijing Normal University for their reviewing this paper.

References

Brown, A., Milton, S., Cullen, M., Golding, B., Mitchell, J., and Shelly, A.: Unified modeling and prediction of weather and climate: A 25-year journey, Bull. Am Meteorol. Soc. 93, 1865–1877, 2012.

Chen, F., and Dudhia, J.: Coupling an advanced land-surface hydrology model with the Penn State-NCAR MM5 modeling system. Part I: Model description and implementation, Mon. Wea. Rev., 129, 569–585, 2001.

Dong, B., Wilcox, L. J., Highwood, E. J., and Sutton, R. T.: Impacts of recent decadal changes in Asian aerosols on the East Asian summer monsoon: roles of aerosol–radiation and aerosol–cloud interactions, Clim. Dyn., 53, 3235-3256, 2019.

Eun, S.-H., Kim, B.-G., Lee, K.-M., and Park, J.-S.: Characteristics of recent severe haze events in Korea and possible inadvertent weather modification, SOLA, 12, 32-36, 2016.

Fan, J., Yuan, T., Comstock, J. M., et al.: Dominant role by vertical wind shear in regulating aerosol effects on deep convective clouds, J. Geophys. Res., 114, doi:10.1029/2009JD012352, 2009.

Fouquart, Y., and Bonnel, B.: Computation of solar heating of the Earth's atmosphere: a new parameterization, Beitr. Phys. Atmos., 53, 35-62, 1980.

Ha, K.-J., Nam, S., Jeong, J.-Y., et al., Observations utilizing Korean ocean research stations and their applications for process studies, Bull. Amer. Meteor. Soc., 100, 2061-2075, 2019.

Holben, B. N., Tanré, D., Smirnov, et al.: An emerging ground-based aerosol climatology: Aerosol optical depth from AERONET, J. Geophys. Res., 106, 12067–12097, 2001.

Houze, R. A., Cloud dynamics, Academic Press, 573 pp, 1993.

Hwang, S.-O., and Lee, D.-K.: A study on the relationship between heavy rainfalls and associated low-level jets in the Korean peninsula, J. Korean. Meteorol. Soc., 29, 133–146, 1993.

Jiang, H., Xue, H., Teller, A., Feingold, G., and Levin, Z.: Aerosol effects on the lifetime of shallow cumulus, Geophys. Res. Lett., 33, L14806, doi:10.1029/2006GL026024, 2006.

1042 Kar, S. K., Lioi, Y.A., and Ha, K.-J. : Aerosol effects on the enhancement of cloud-to-
1043 ground lightning over major urban areas of South Korea, Atmos. Res. , 92, 80-87,
1044 2009.
1045 Khain, A., BenMoshe, N., and Pokrovsky, A.: Factors determining the impact of aerosols
1046 on surface precipitation from clouds: Attempt of classification, J. Atmos. Sci., 65,
1047 1721-1748, 2008.
1048 Khain, A., Pokrovsky, A., Rosenfeld, D., Blahak, U., and Ryzhkoy, A.: The role of CCN in
1049 precipitation and hail in a mid-latitude storm as seen in simulations using a spectral
1050 (bin) microphysics model in a 2D dynamic frame, Atmos. Res., 99, 129–146, 2011.
1051 Khain, A., Rosenfeld, D., and Pokrovsky, A.: Aerosol impact on the dynamics and
1052 microphysics of deep convective clouds, Quart. J. Roy. Meteor. Soc., 131, 2639-266,
1053 2005.
1054 Khain, A. D., BenMoshe, N., and A. Pokrovsky, A.: Factors determining the impact of
1055 aerosols on surface precipitation from clouds: An attempt at classification, J. Atmos.
1056 Sci., 65, 1721–1748, doi:10.1175/2007JAS2515.1, 2008.
1057 King, J.: Automatic weather stations, available at
1058 https://web.archive.org/web/20090522121225/http://www.automaticweatherstation.c
1059 om/index.html, 2009.
1060 Koop, T., Luo, B. P., Tsias, A., and Peter, T.: Water activity as the determinant for
1061 homogeneous ice nucleation in aqueous solutions, Nature, 406, 611-614, 2000.
1062 Lebo, Z. J., and Morrison, H.: Dynamical effects of aerosol perturbations on simulated
1063 idealized squall lines, Mon. Wea. Rev., 142, 991-1009, 2014.
1064 Lee, D.-K., Kim, H.-R., and Hong, S.-Y.: Heavy rainfall over Korea during 1980–1990.
1065 Korean, J. Atmos. Sci., 1, 32–50, 1998.
1066 Lee, S., Ho, C.-H., Lee, Y. G., Choi, H.-J. and Song, C.-K.: Influence of transboundary air
1067 pollutants from China on the high-PM10 episode in Seoul, Korea for the period
1068 October 16−20, 2008. Atmos. Environ., 77, 430−439, 2013.
1069 Lee, S. S., Donner, L. J., Phillips, V. T. J., and Ming, Y.: The dependence of aerosol effects
1070 on clouds and precipitation on cloud-system organization, shear and stability, J.
1071 Geophys. Res., 113, D16202, 2008.
1072 Lee, S. S., Kim, B.-G., and Yum, S. S., et al.: Effect of aerosol on evaporation, freezing and

precipitation in a multiple cloud system, Clim. Dyn., 48, 1069-1087, 2016.

Lee, S. S., Li, Z., Mok, J., et al,: Interactions between aerosol absorption, thermodynamics, dynamics, and microphysics and their impacts on clouds and precipitation in a multiple-cloud system, Clim. Dyn., https://doi.org/10.1007/s00382-017-3552-x, 2017.

Lee, S. S., Kim, B.-G., Li, Z., Choi, Y.-S., Jung, C.-H., Um, J., Mok, J., and Seo, K.-H.: Aerosol as a potential factor to control the increasing torrential rain events in urban areas over the last decades, Atmos. Chem. Phys., 18, 12531–12550, https://doi.org/10.5194/acp-18-12531-2018, 2018.

Li, Z., Niu, F., Fan, J., Liu, Y., Rosenfeld, D., and Ding, Y.: Long-term impacts of aerosols on the vertical development of clouds and precipitation, Nat. Geosci., 4, 888-894, 2011.

Lohmann, U. and Diehl, K.: Sensitivity studies of the importance of dust ice nuclei for the indirect aerosol effect on stratiform mixed-phase clouds, J. Atmos. Sci., 63, 968-982, 2006.

Lu, Z., Zhang, Q., and Streets, D. G.: Sulfur dioxide and primary carbonaceous aerosol emissions in China and India, 1996–2010, Atmos. Chem. Phys., 11, 9839–9864, 2011.

Mlawer, E. J., Taubman, S. J., Brown, P. D., Iacono, M. J., and Clough, S. A.: RRTM, a validated correlated-k model for the longwave, J. Geophys. Res., 102, 16663-1668, 1997.

Möhler, O., et al, Efficiency of the deposition mode ice nucleation on mineral dust particles, Atmos. Chem. Phys., 6, 3007-3021, 2006.

Morrison, H., and Grabowski, W. W.: Cloud-system resolving model simulations of aerosol indirect effects on tropical deep convection and its thermodynamic environment, Atmos. Chem. Phys., 11, 10503–10523, 2011.

Oh, H., Ha, K.-J. and Timmermann, A.: Disentangling Impacts of Dynamic and Thermodynamic Components on Late Summer Rainfall Anomailes in East Asia, J. Geophys. Res., 123, 8623-8633, 2018.

Oh, H.-R., Ho, C.-H., Kim, J., Chen, D., Lee, S., Choi, Y.-S., Chang, L.-S., and Song, C.-K.: Long-range transport of air pollutants originating in China: A possible major cause of multi-day high-PM10 episodes during cold season in Seoul, Korea. Atmos.

Environ., 109, 23−30, 2015.

Pruppacher, H. R. and Klett, J. D.: Microphysics of clouds and precipitation, 714pp, D. Reidel, 1978.

Rosenfeld, D., Lohmann, U., Raga, G. B., et al.: Flood or drought, How do aerosols affect precipitation? Science, 321, 1309-1313, 2008.

Storer, R. L., van den Heever, S. C., and Stephens, G. L.: Modeling aerosol impacts on convection under differing storm environments, J. Atmos. Sci., 67, 3904-3915, 2010.

Seo, K.-H., Son, J. H., Lee, J.-H., and Park, H.-S.: Northern East Asian monsoon precipitation revealed by air mass variability and its prediction, J. Clim., 28, 6221-6233, 2013.

Tao, W.-K., Chen, J.-P., Li, Z., Wang, C., and Zhang, C.: Impact of aerosols on convective clouds and precipitation, Rev. Geophys., 50, RG2001, 2012.

Tao, W. K., Cloud resolving modeling, J. Meteorol. Soc. Jpn., 85B, 305–330, doi:10.2151/jmsj.85B.305, 2007.

van den Heever, S. C., Carrió, G. G., Cotton, W. R., DeMott, P. J., and Prenni, A. J.: Impacts of nucleating aerosol on Florida storms. part I: Mesoscale simulations, J. Atmos. Sci., 63, 1752–1775, 2006.

Wang, H., Skamarock, W. C., and Feingold, G.: Evaluation of scalar advection schemes in the Advanced Research WRF model using large-eddy simulations of aerosol-cloud interactions, Mon. Wea. Rev., 137, 2547-2558, 2009.

Weisman, M. L., and Klemp, J. B.: The dependence of numerically simulated convective storms on vertical wind shear and buoyancy, Mon. Wea. Rev., 110, 504-520, 1982.

FIGURE CAPTIONS

Figure 1. Wind (m s^{-1}), equivalent potential temperature (K), and geopotential height (m) at 850 hPa level over Northeast Asia at (a) 21:00 LST December 23rd 2017 and (b) 09:00 LST July 27th 2015. Wind, equivalent potential temperature, and geopotential height are represented by arrows, a shaded field, and contours, respectively. An inner rectangle in the Korean Peninsula in (a) marks the Seoul area and that in the East-Asia continent in (b) marks the Beijing area.

Figure 2. Inner rectangles in (a) and (b) mark the Seoul area in the Korean Peninsula and the Beijing area in the East-Asia continent, respectively. A dot outside the inner rectangle in (a) marks Baekryongdo island. Dots in the inner rectangles in (a) and (b) mark the selected locations where precipitation and aerosol mass are measured. In (a) and (b), the light blue represents the ocean and the green the land area.

Figure 3. Surface size distribution of aerosols (a) for the Seoul case and (b) for the Beijing case. Aerosol number concentration per unit volume of air is represented by N and aerosol diameter by D.

Figure 4. Time series of $PM_{2.5}$ observed at the ground station in Baekryongdo island (blue line) and of the average $PM_{2.5}$ over ground stations in the Seoul area (red line) between 07:00 LST on December 22nd and 21:00 LST on December 24th in 2017. Note that $PM_{2.5}$ observed at stations in the Seoul area is applied to the control-s run whose period is marked by the dashed rectangle. Time series of the average $PM_{2.5}$ over stations in the Seoul area in the low-aerosol-s run for the simulation period is also shown (black solid line).

Figure 5. Time series of precipitation rates at the surface, which are averaged over the domain and smoothed over 1 hour, (a) for the control-s and low-aerosol-s runs in the Seoul area and (b) for the control-b and low-aerosol-b runs in the Beijing area. In (a) and (b), the

averaged and observed precipitation rates over the observation sites in the Seoul and Beijing areas, respectively, are also shown.

Figure 6. Observed and simulated cumulative frequency distributions of precipitation rates at the surface for (a) the Seoul case, which are collected over the Seoul area, and (b) the Beijing case, which are collected over the Beijing area, at the last time step. Simulated distributions are in the control-s and low-aerosol-s runs for the Seoul case and in the control-b and low-aerosol-b runs for the Beijing case. The observed distribution is obtained by interpolating and extrapolating the observed precipitation rates to grid points and time steps in the control-s and control-b runs for the Seoul and Beijing cases, respectively.

Figure 7. Cumulative frequency distributions of the precipitation rates at the surface in the control-s and low-aerosol-s runs for the Seoul case at (a) 06:00, (b) 10:00 and (c) 12:00 LST.

Figure 8. Vertical distributions of differences in the area-averaged condensation, deposition and freezing rates, and cloud-liquid, raindrop, snow and hail mass density, and updraft mass fluxes between the control-s and low-aerosol-s runs at (a) 03:20, (b) 03:40, (c) 06:00 and (d) 12:00 LST. The horizontal black line in each panel represents the altitude of freezing or melting. Here, for the sake of the display brevity, snow mass density includes ice-mass density, while hail mass density includes graupel mass density.

Figure 9. Spatial distributions of terrain heights, column-averaged condensation rates, surface wind vectors and precipitation rates at (a) and (b) 03:40, (c) and (d) 07:20, (e) and (f) 08:40, (g) and (h) 10:00, (i) and (j) 11:00, and (k) and (l)12:00. The distributions in the control-s run are shown in (a), (c), (e), (g), (i) and (k), and the distributions in the low-aerosol-s run are shown in (b), (d), (f), (h), (j) and (l). Condensation rates are shaded. Dark-yellow and dark-red contours represent precipitation rates at 0.5 and 3.0 mm hr^{-1}, respectively, while beige, light brown and brown contours represent terrain heights at 100, 300 and 600 m, respectively. See text for yellow rectangles in (a), (b), (g) and (h)

Figure 10. Cumulative frequency distributions of the column-averaged condensation rates in the control-s and low-aerosol-s runs for the Seoul case at (a) 07:20 and (b) 09:00 LST.

Figure 11. Cumulative frequency distributions of the precipitation rates at the surface in the control-b and low-aerosol-b runs for the Beijing case at (a) 16:00, (b) 17:00, (c) 17:20, and (d) 19:00 LST.

Figure 12. Same as Figure 8 but for differences between the control-b and low-aerosol-b runs at (a) 14:20, (b) 15:40, (c) 16:00, (d) 17:20 and (e) 19:00 LST.

Figure 13. Spatial distributions of terrain heights, column-averaged condensation rates, surface wind vectors and precipitation rates at (a) and (b) 14:20, and (c) and (d) 17:20 LST. (a) and (c) are for the control-b run and (b) and (d) are for the low-aerosol-b run. Condensation rates are shaded. Dark-yellow and dark-red contours represent precipitation rates at 1.0 and 2.0 mm hr^{-1}, respectively, while beige, light brown, brown and dark brown contours represent terrain heights at 100, 500, 1000 and 1500 m, respectively. See text for yellow circles in (a) and (b).

Figure 14. Cumulative frequency distributions of the column-averaged condensation rates in the control-b and low-aerosol-b runs for the Beijing case at (a) 17:20 and (b) 19:00 LST.

Figure 15. Mean precipitation rates corresponding to each column-averaged condensation rate for the period between 14:00 and 17:20 LST in the control-b run. One standard deviation of precipitation rates is represented by a vertical bar at each condensation rate.

Figure 16. Spatial distributions of precipitation rates (shaded) and wind vectors (arrows) for the Beijing case at (a) and (b) 17:00, (c) and (d) 17:20, (e) and (f) 17:40, (g) and (h) 18:00, (i) and (j) 18:20, (k) and (l) 18:40, and (m) and (n) 19:00 LST. The distributions in the control-b run are in (a), (c), (e), (g), (i), (k) and (m). The distributions in the low-aerosol-b run are in (b), (d), (f), (h), (j), (l) and (n).

Figure 17. Vertical distributions of (a) the area-averaged cloud-liquid and rain evaporation rates and (b) downdraft mass fluxes in the control-b and low-aerosol-b runs over a period from 17:00 to 19:00 LST.

Simulations	Site	Concentrations of background aerosols acting as CCN
Control-s run	Seoul area	Observed and affected by the aerosol advection
Low-aerosol-s run	Seoul area	Same as those in the control-s run but unaffected by the aerosol advection
Control-b run	Beijing area	Observed
Low-aerosol-b run	Beijing area	Reduced by a factor of 3.1 as compared to those observed

Table 1. Summary of simulations

Simulations	The net flux of the moist static energy which crosses the boundary between areas A and B ($J\ m^{-2}\ s^{-1}$)	
	At 16:30 LST	16:30 to 17:00 LST
Control-b run	1.57×10^{12}	1.07×10^{15}
Low-aerosol-b run	1.15×10^{12}	7.55×10^{14}

Table 2. The net flux of the moist static energy which crosses the boundary between areas A and B at 16:30 LST and for a period from 16:30 to 17:00 LST.

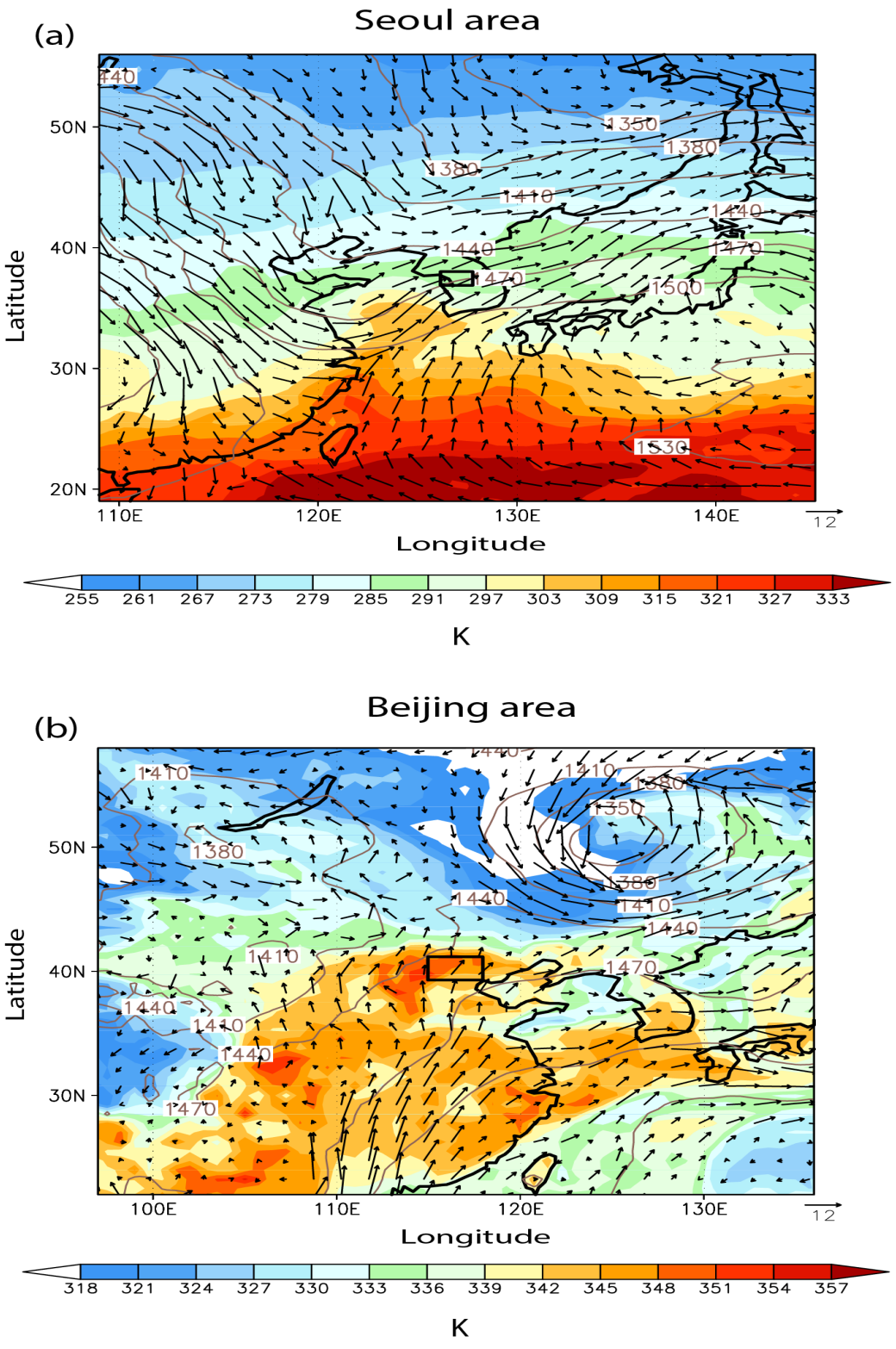
(a)
Seoul area
50N
40N
30N
20N
Latitude
110E
120E
130E
140E
Longitude
1350
1380
1410
1440
1470
1500
1530
255 261 267 273 279 285 291 297 303 309 315 321 327 333
K
(b)
Beijing area
50N
40N
30N
Latitude
100E
110E
120E
130E
Longitude
1350
1380
1410
1440
1470
318 321 324 327 330 333 336 339 342 345 348 351 354 357
K

Figure 1

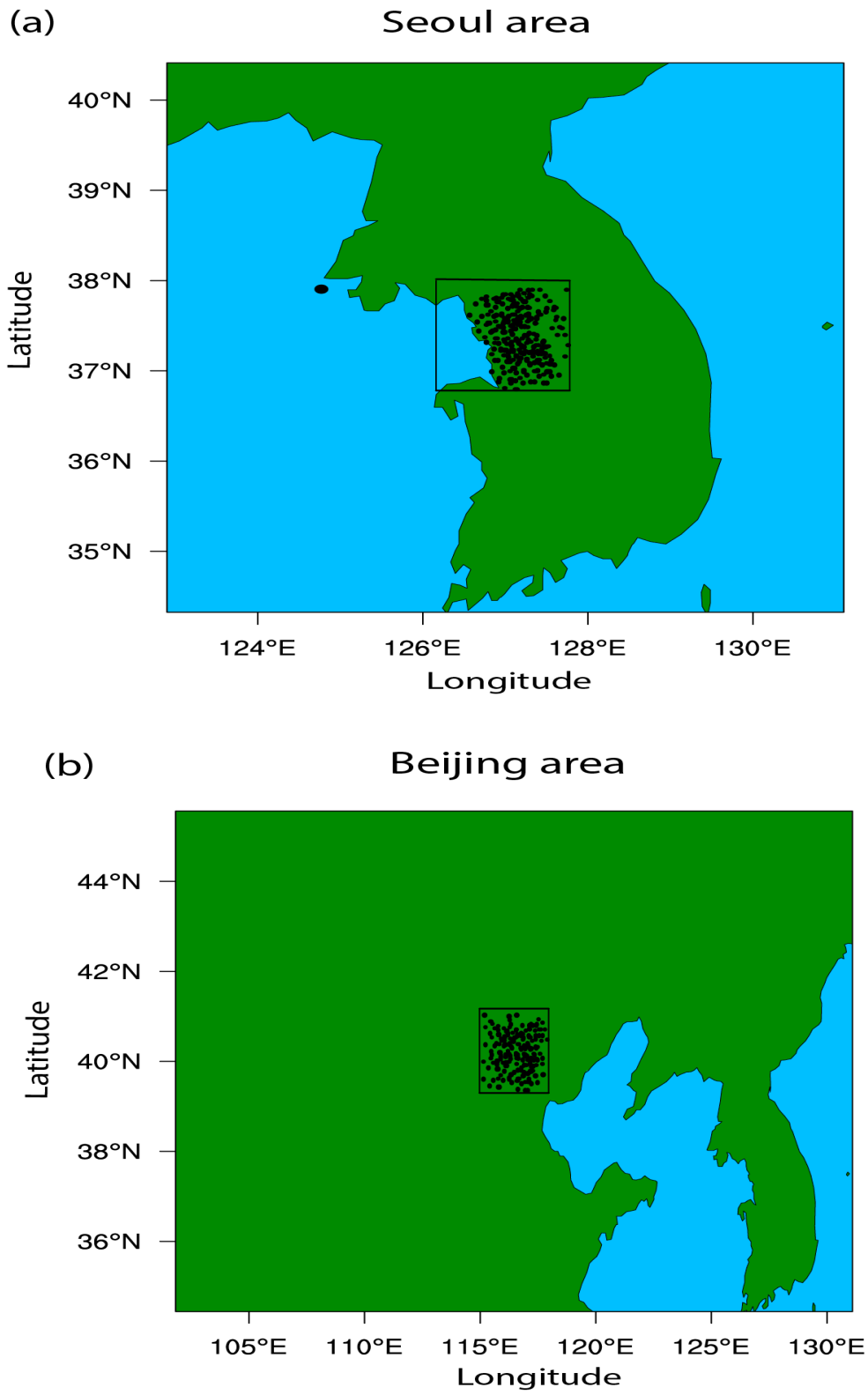

1276

1277 **Figure 2**

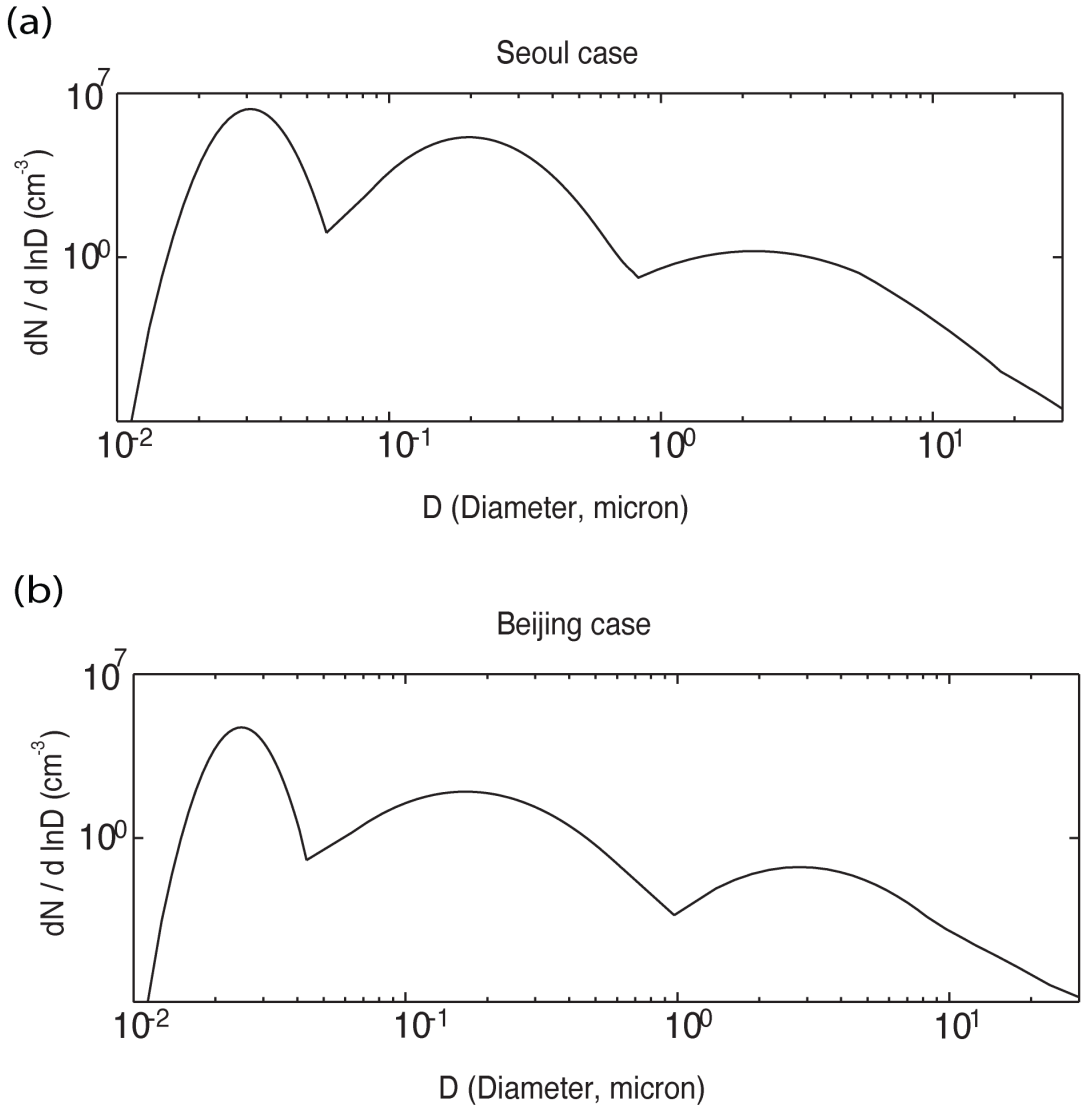
(a)
Seoul case
dN / d lnD (cm-3)
D (Diameter, micron)
(b)
Beijing case
dN / d lnD (cm-3)
D (Diameter, micron)

Figure 3

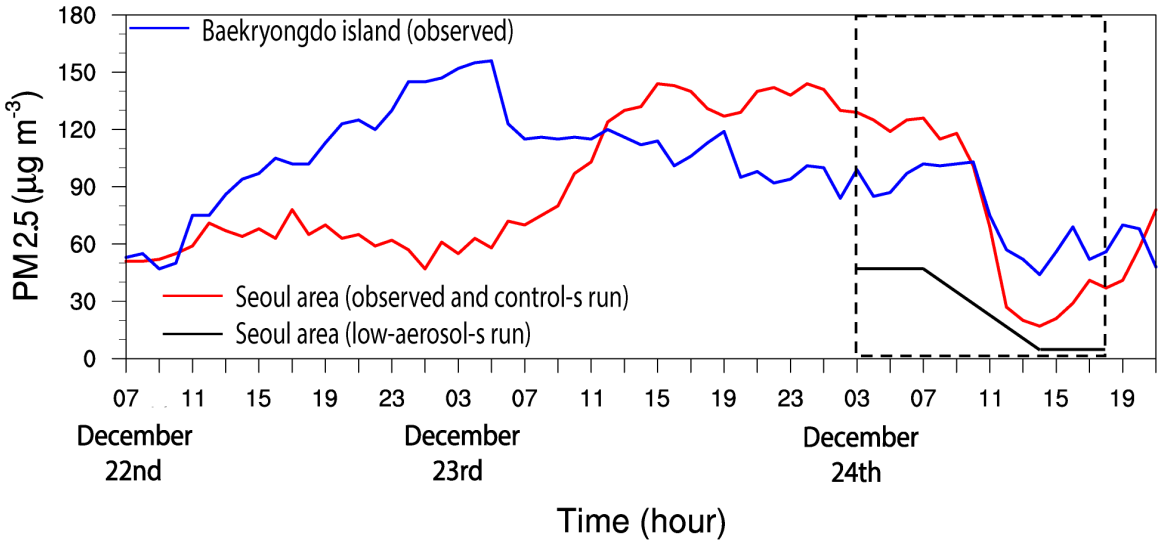

1285

1286 **Figure 4**

1287

1288

1289

1290

1291

1292

1293

1294

1295

1296

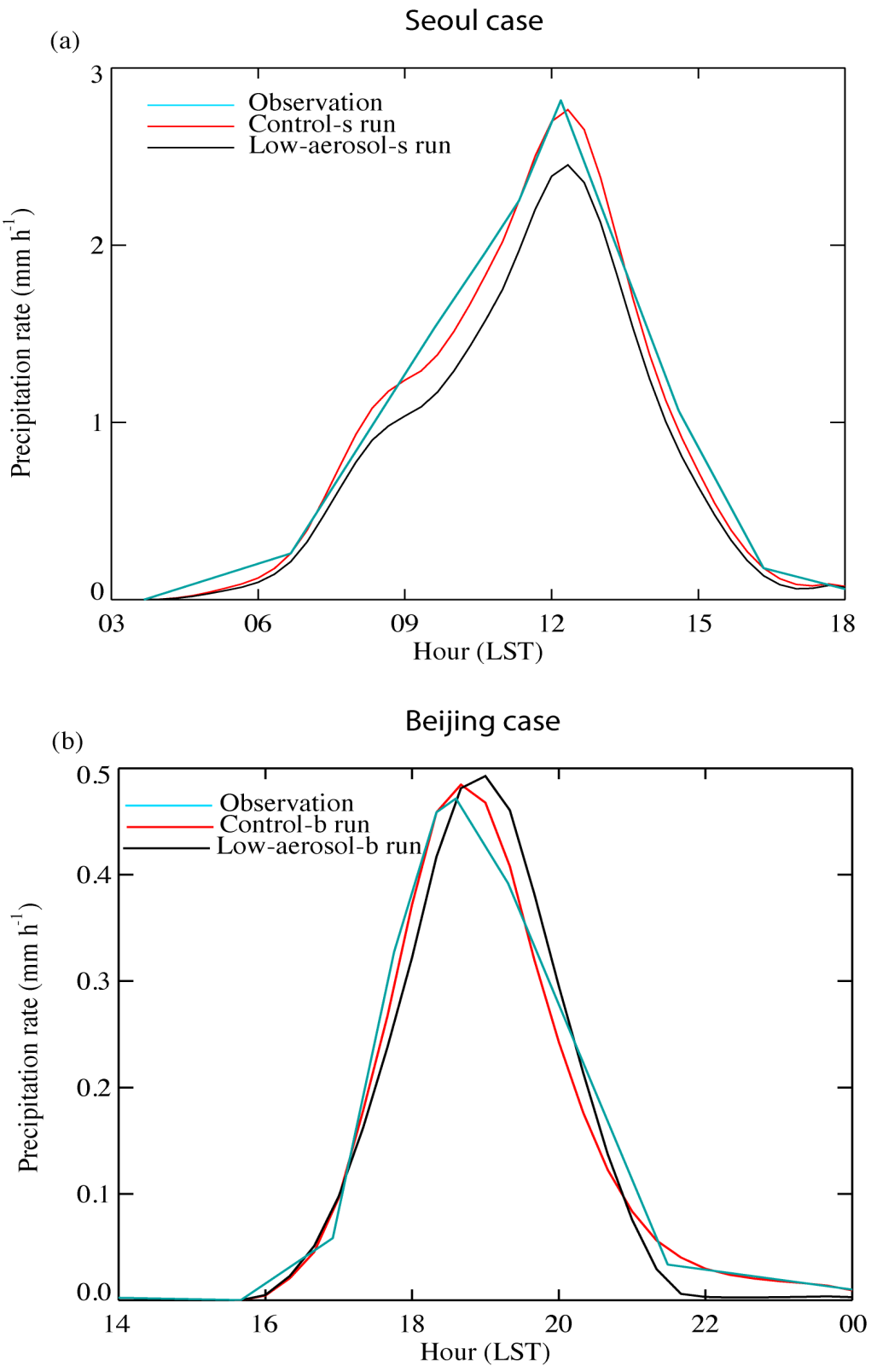

1297

1298 **Figure 5**

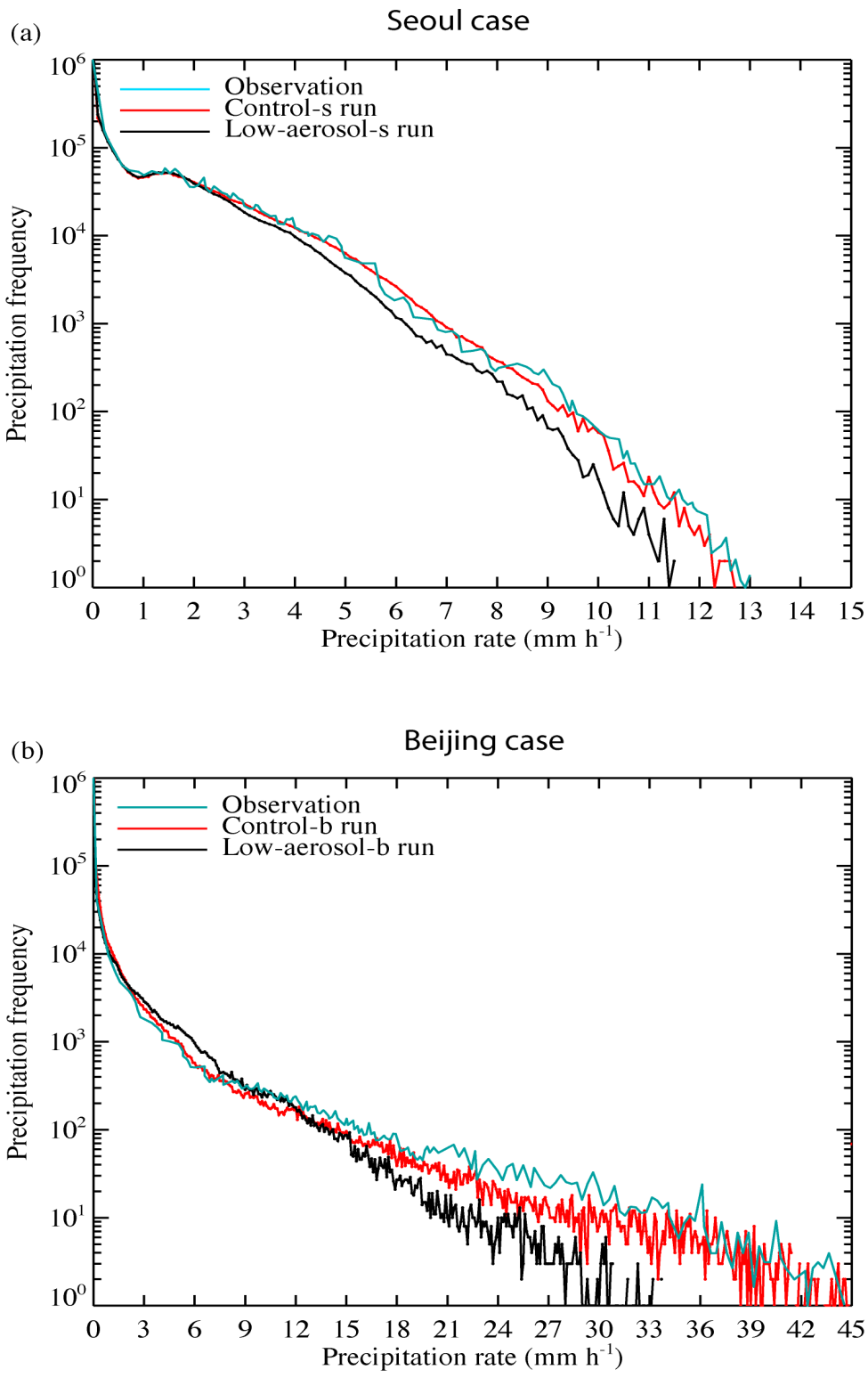

1299

1300 **Figure 6**

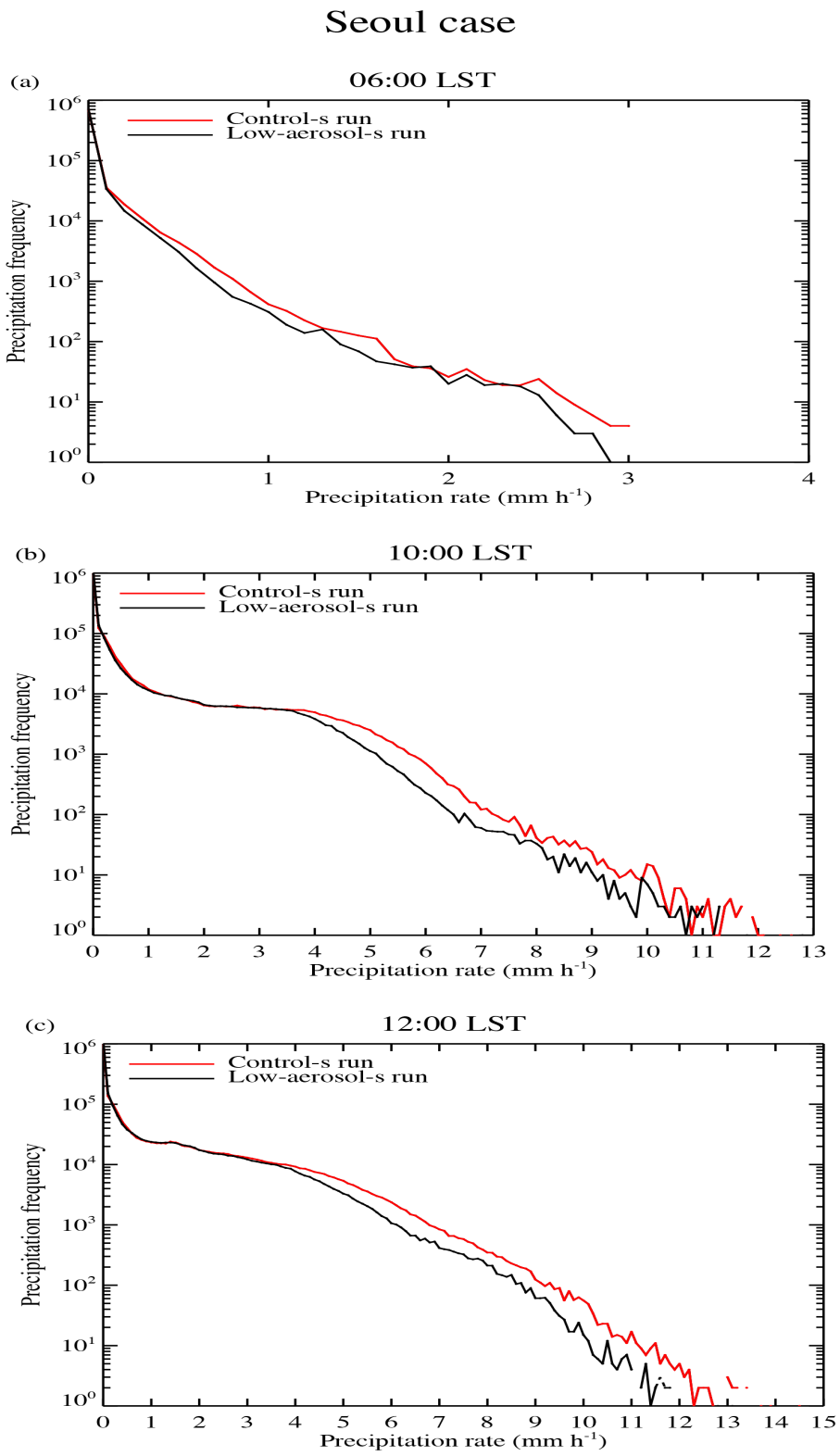

1301

1302 **Figure 7**

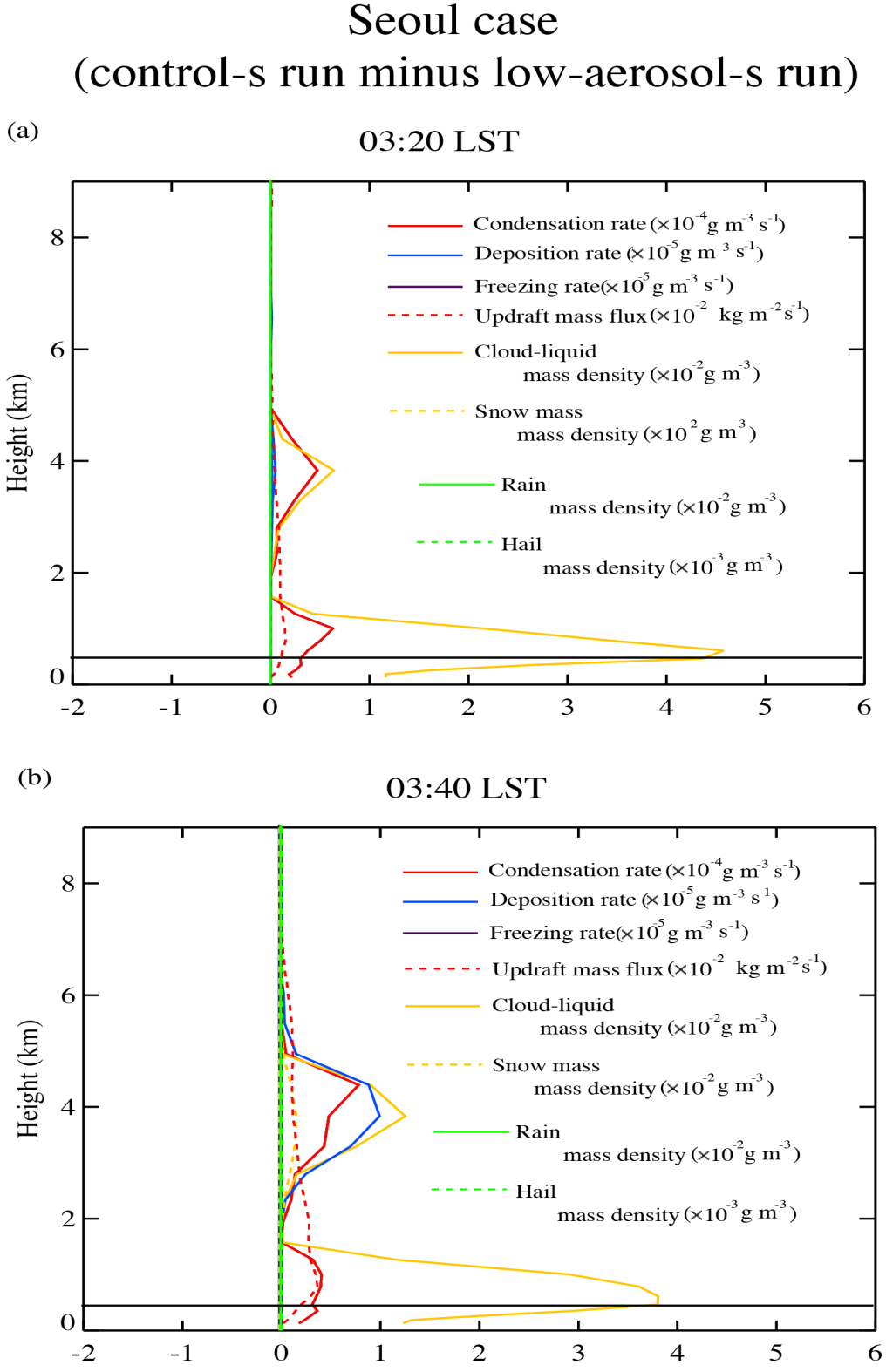
Seoul case
(control-s run minus low-aerosol-s run)
(a)
03:20 LST
Height (km)
Condensation rate (×10-4 g m-3 s-1)
Deposition rate (×10-5 g m-3 s-1)
Freezing rate(×10-5 g m-3 s-1)
Updraft mass flux (×10-2 kg m-2 s-1)
Cloud-liquid mass density (×10-2 g m-3)
Snow mass mass density (×10-2 g m-3)
Rain mass density (×10-2 g m-3)
Hail mass density (×10-3 g m-3)
(b)
03:40 LST
Height (km)
Condensation rate (×10-4 g m-3 s-1)
Deposition rate (×10-5 g m-3 s-1)
Freezing rate(×10-5 g m-3 s-1)
Updraft mass flux (×10-2 kg m-2 s-1)
Cloud-liquid mass density (×10-2 g m-3)
Snow mass mass density (×10-2 g m-3)
Rain mass density (×10-2 g m-3)
Hail mass density (×10-3 g m-3)

Figure 8

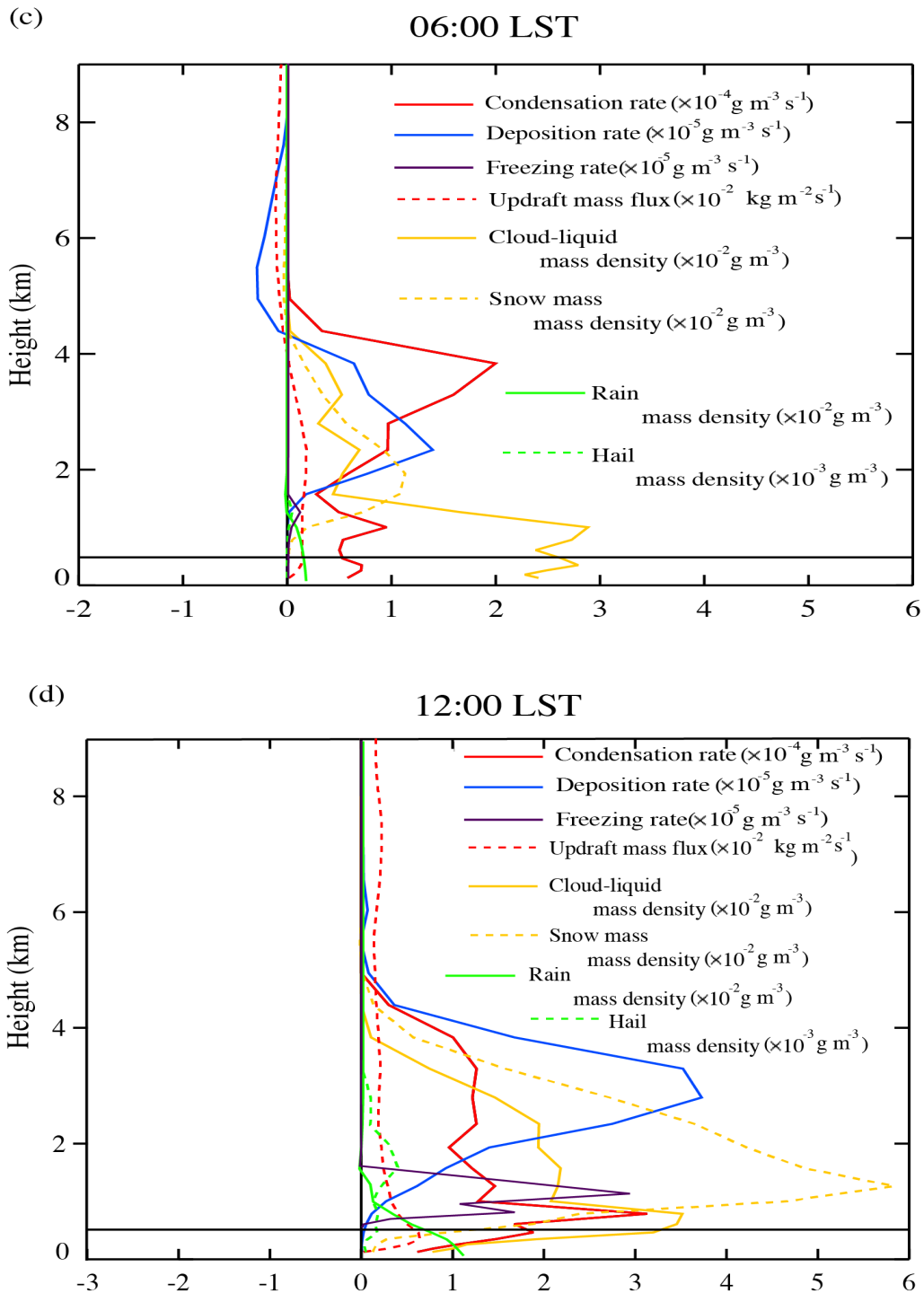
(c)
06:00 LST
Height (km)
Condensation rate (×10⁻⁴ g m⁻³ s⁻¹)
Deposition rate (×10⁻⁵ g m⁻³ s⁻¹)
Freezing rate(×10⁻⁵ g m⁻³ s⁻¹)
Updraft mass flux (×10⁻² kg m⁻² s⁻¹)
Cloud-liquid mass density (×10⁻² g m⁻³)
Snow mass mass density (×10⁻² g m⁻³)
Rain mass density (×10⁻² g m⁻³)
Hail mass density (×10⁻³ g m⁻³)
(d)
12:00 LST
Height (km)
Condensation rate (×10⁻⁴ g m⁻³ s⁻¹)
Deposition rate (×10⁻⁵ g m⁻³ s⁻¹)
Freezing rate(×10⁻⁵ g m⁻³ s⁻¹)
Updraft mass flux (×10⁻² kg m⁻² s⁻¹)
Cloud-liquid mass density (×10⁻² g m⁻³)
Snow mass mass density (×10⁻² g m⁻³)
Rain mass density (×10⁻² g m⁻³)
Hail mass density (×10⁻³ g m⁻³)

Figure 8

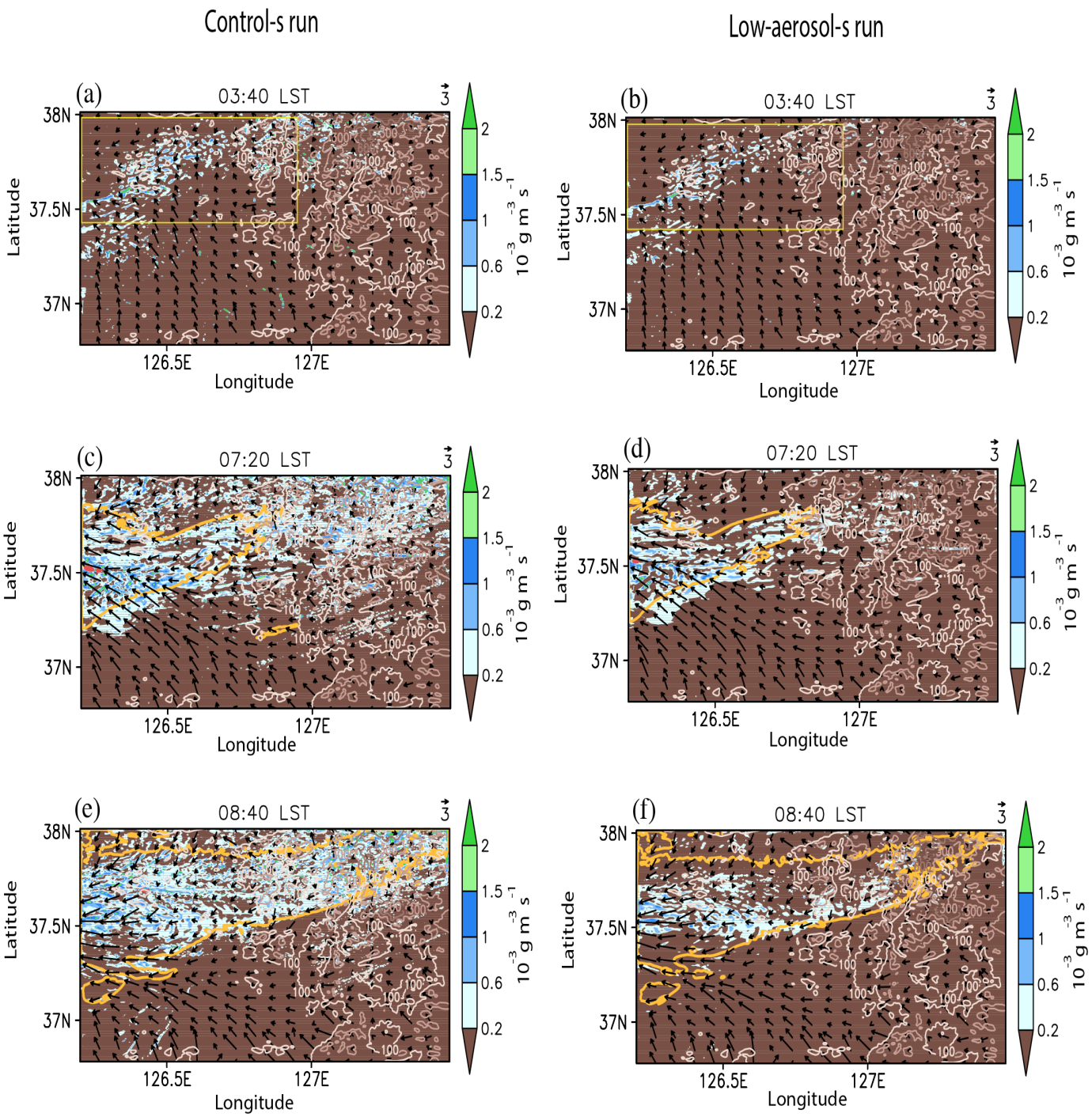

1308

1309 **Figure 9**

1310

1311

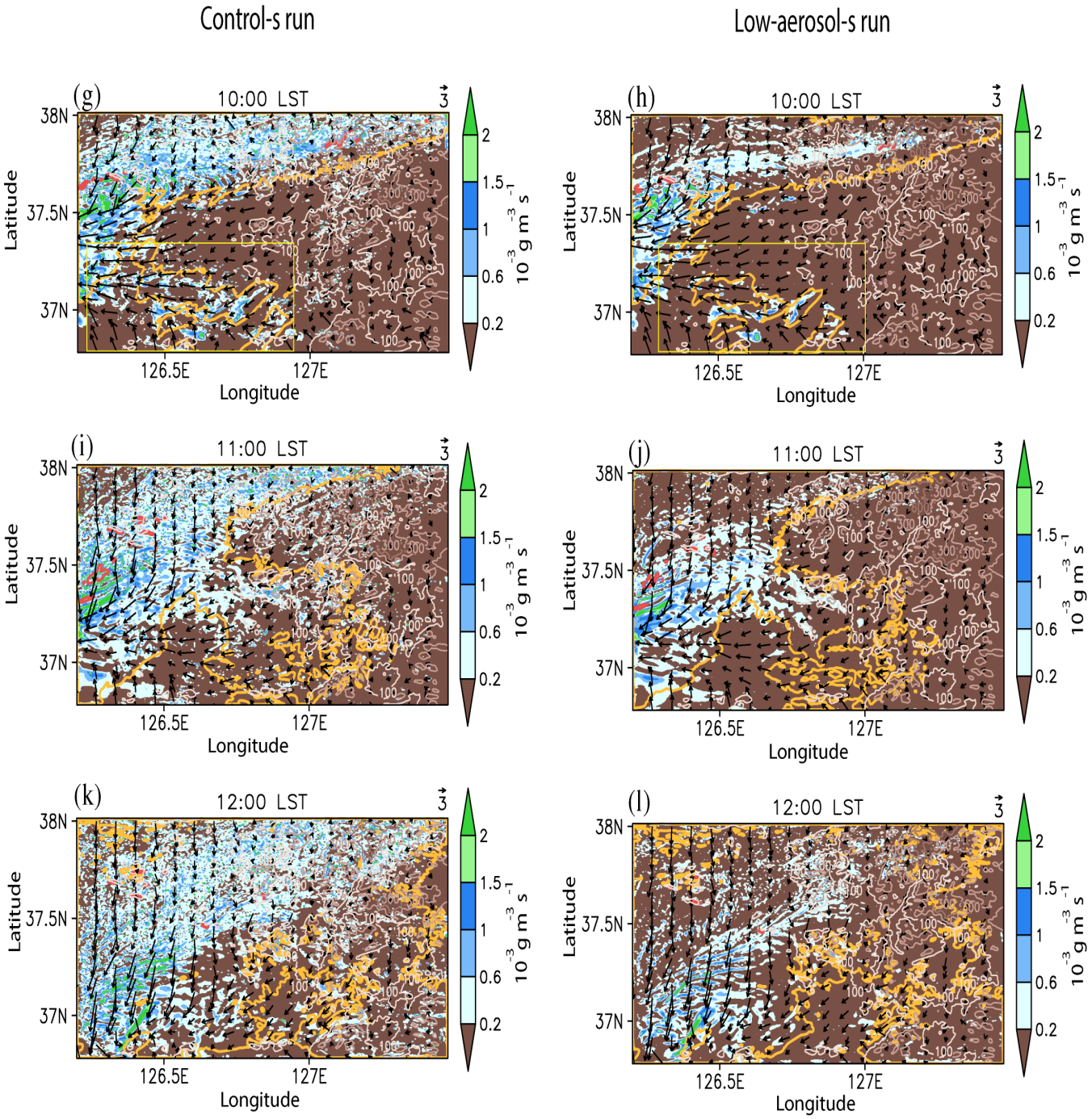

1312

1313 **Figure 9**

1314

1315

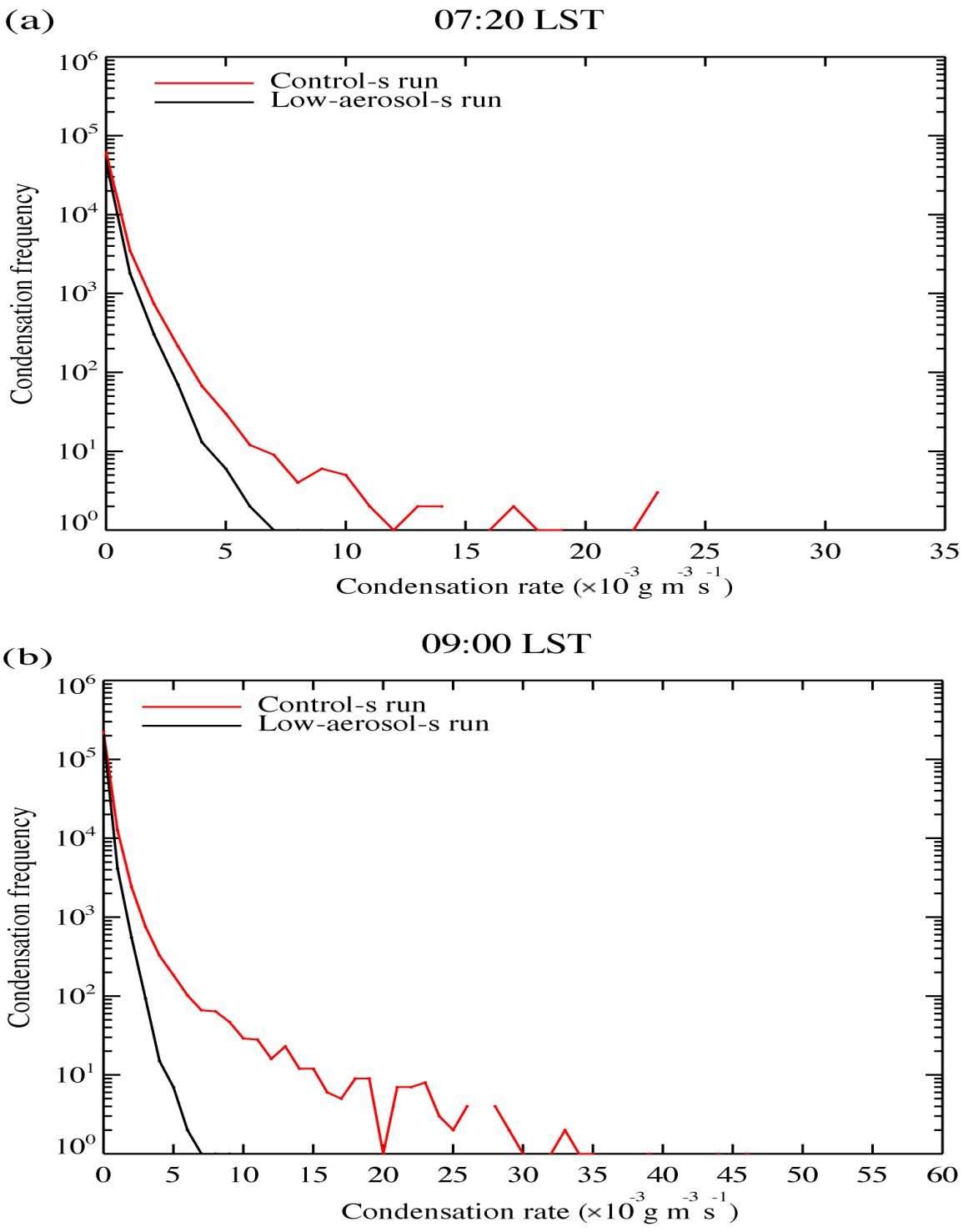
Seoul case
(a)
07:20 LST
Control-s run
Low-aerosol-s run
Condensation frequency
Condensation rate (×10^-3 g m^-3 s^-1)
(b)
09:00 LST
Control-s run
Low-aerosol-s run
Condensation frequency
Condensation rate (×10^-3 g m^-3 s^-1)

Figure 10

Beijing case

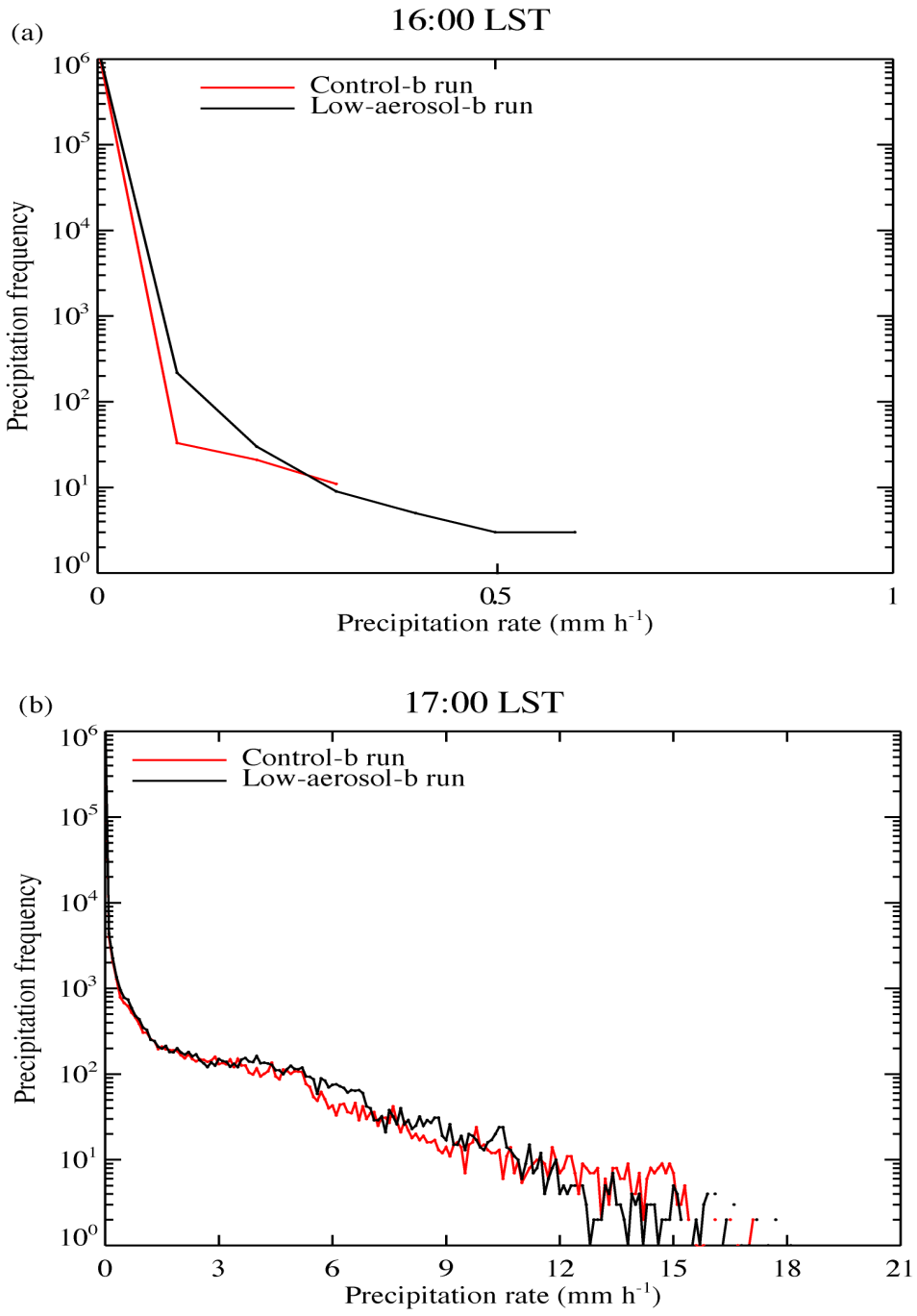

1319

1320 **Figure 11**

1321

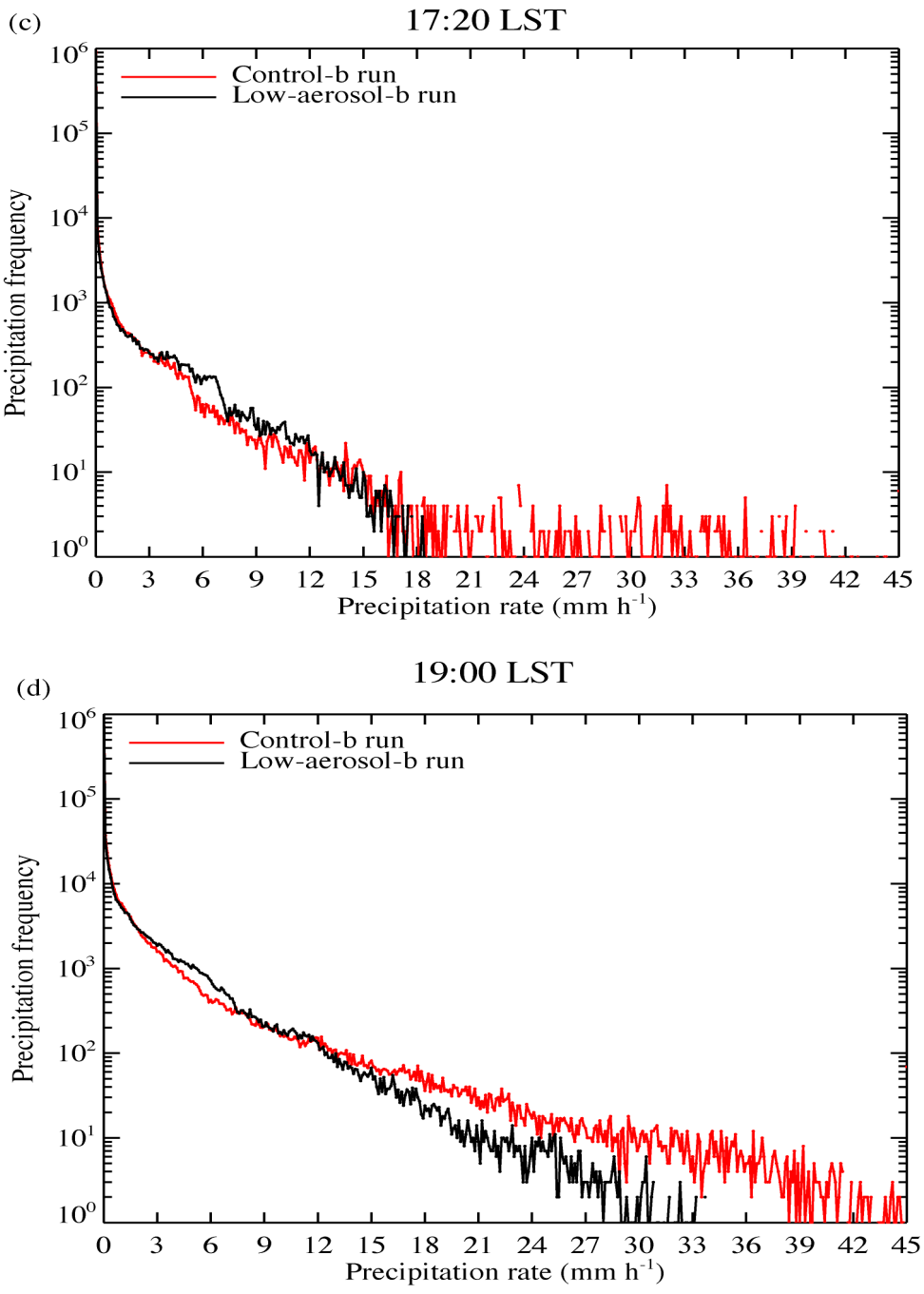
(c)
17:20 LST
Control-b run
Low-aerosol-b run
Precipitation frequency
Precipitation rate (mm h-1)
(d)
19:00 LST
Control-b run
Low-aerosol-b run
Precipitation frequency
Precipitation rate (mm h-1)

Figure 11

Beijing case
(control-b run minus low-aerosol-b run)

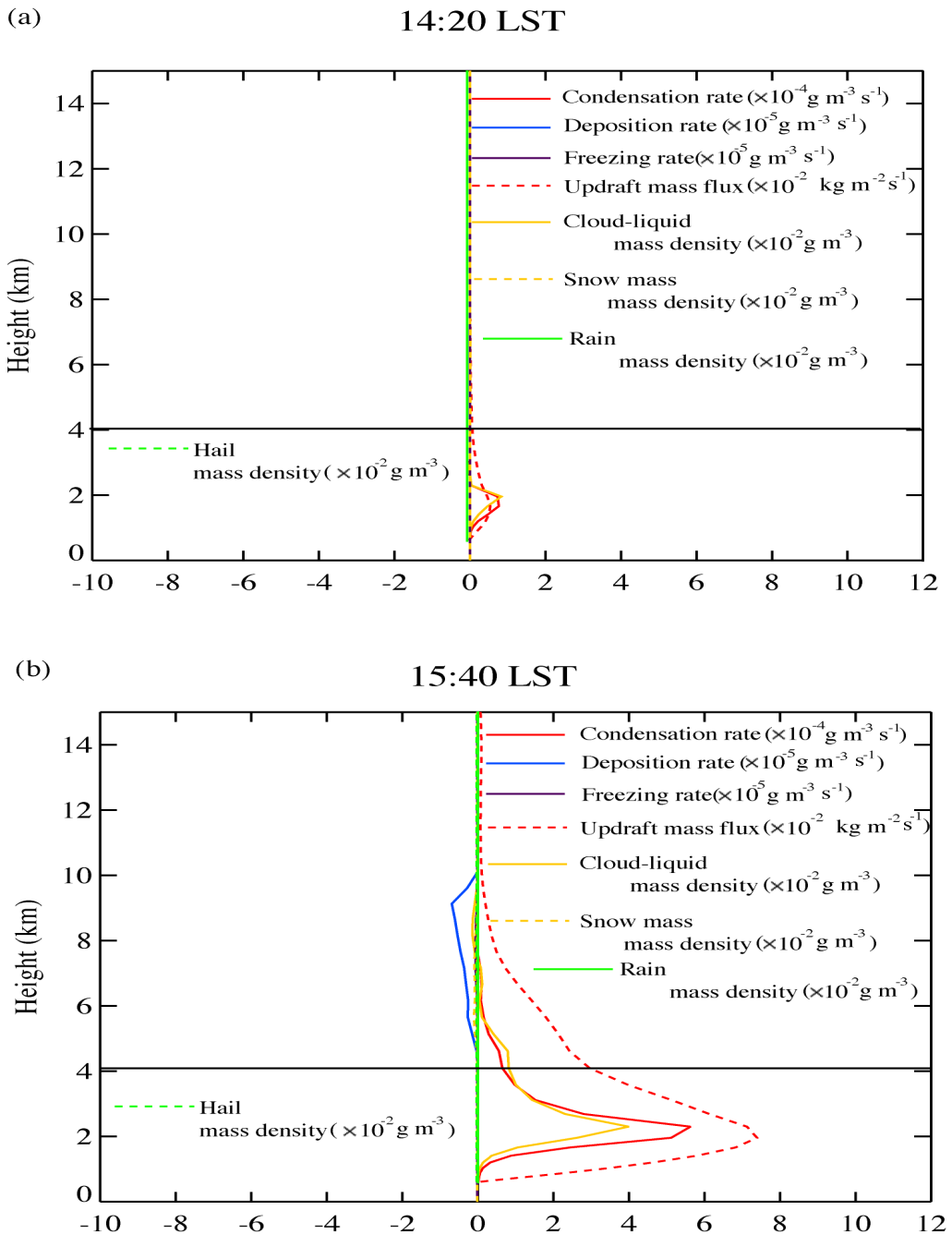

Figure 12

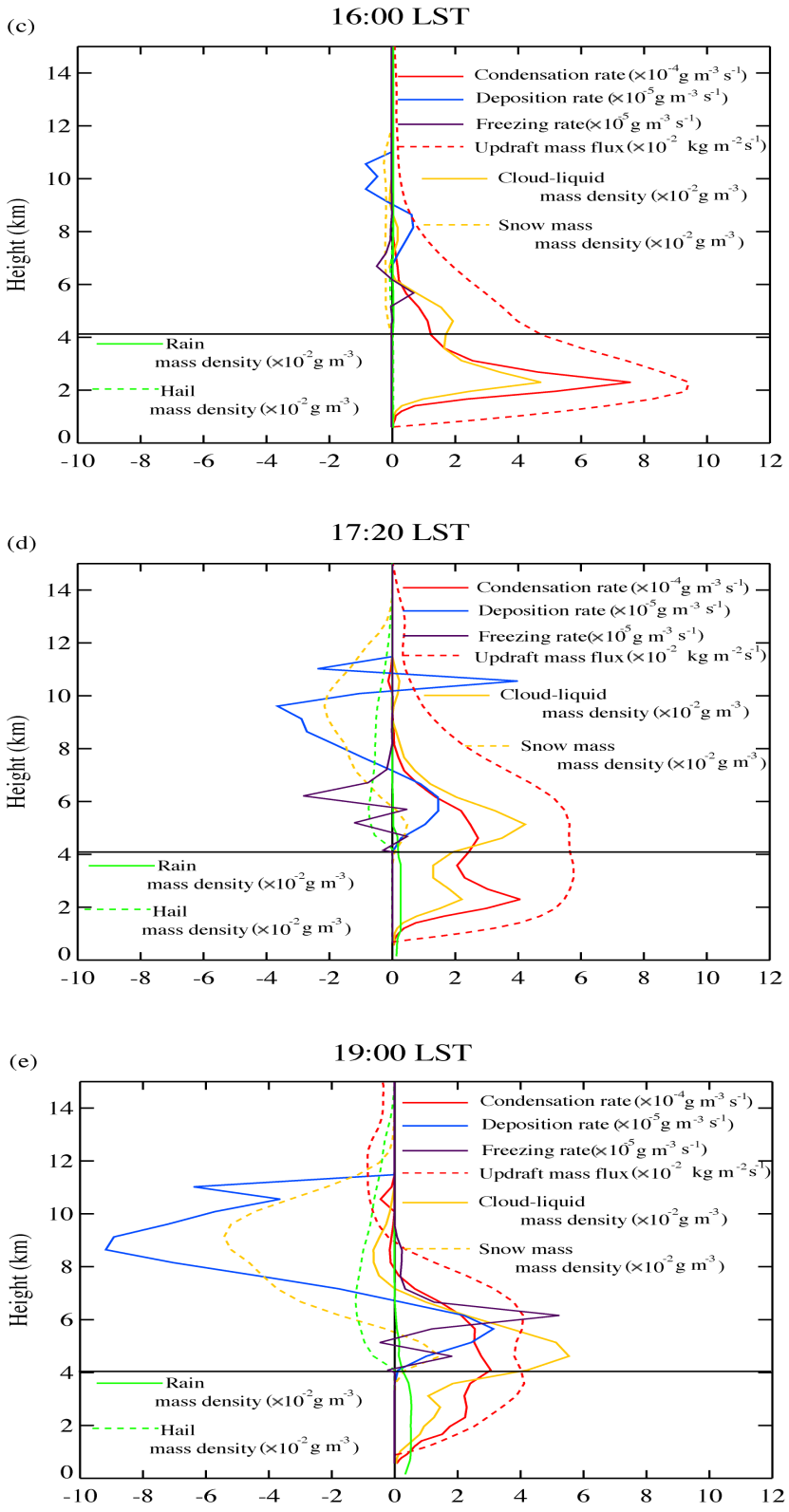
(c)
16:00 LST
(d)
17:20 LST
(e)
19:00 LST
Height (km)
Condensation rate (×10⁻⁴ g m⁻³ s⁻¹)
Deposition rate (×10⁻⁵ g m⁻³ s⁻¹)
Freezing rate(×10⁻⁵ g m⁻³ s⁻¹)
Updraft mass flux (×10⁻² kg m⁻² s⁻¹)
Cloud-liquid mass density (×10⁻² g m⁻³)
Snow mass mass density (×10⁻² g m⁻³)
Rain mass density (×10⁻² g m⁻³)
Hail mass density (×10⁻² g m⁻³)

Figure 12

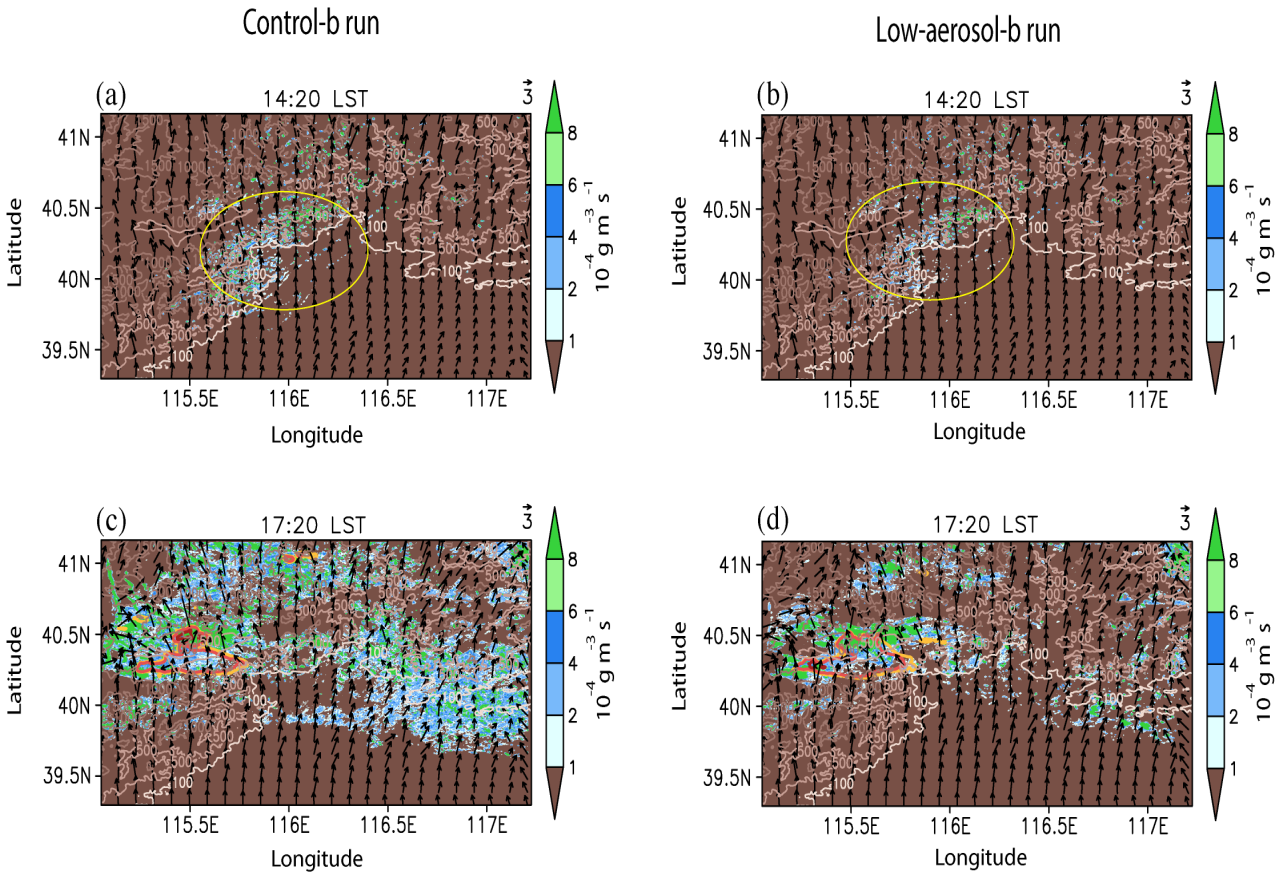
Control-b run
Low-aerosol-b run
(a)
14:20 LST
(b)
14:20 LST
(c)
17:20 LST
(d)
17:20 LST
Latitude
Longitude
41N
40.5N
40N
39.5N
115.5E
116E
116.5E
117E
10 g m s
-4 -3 -1

Figure 13

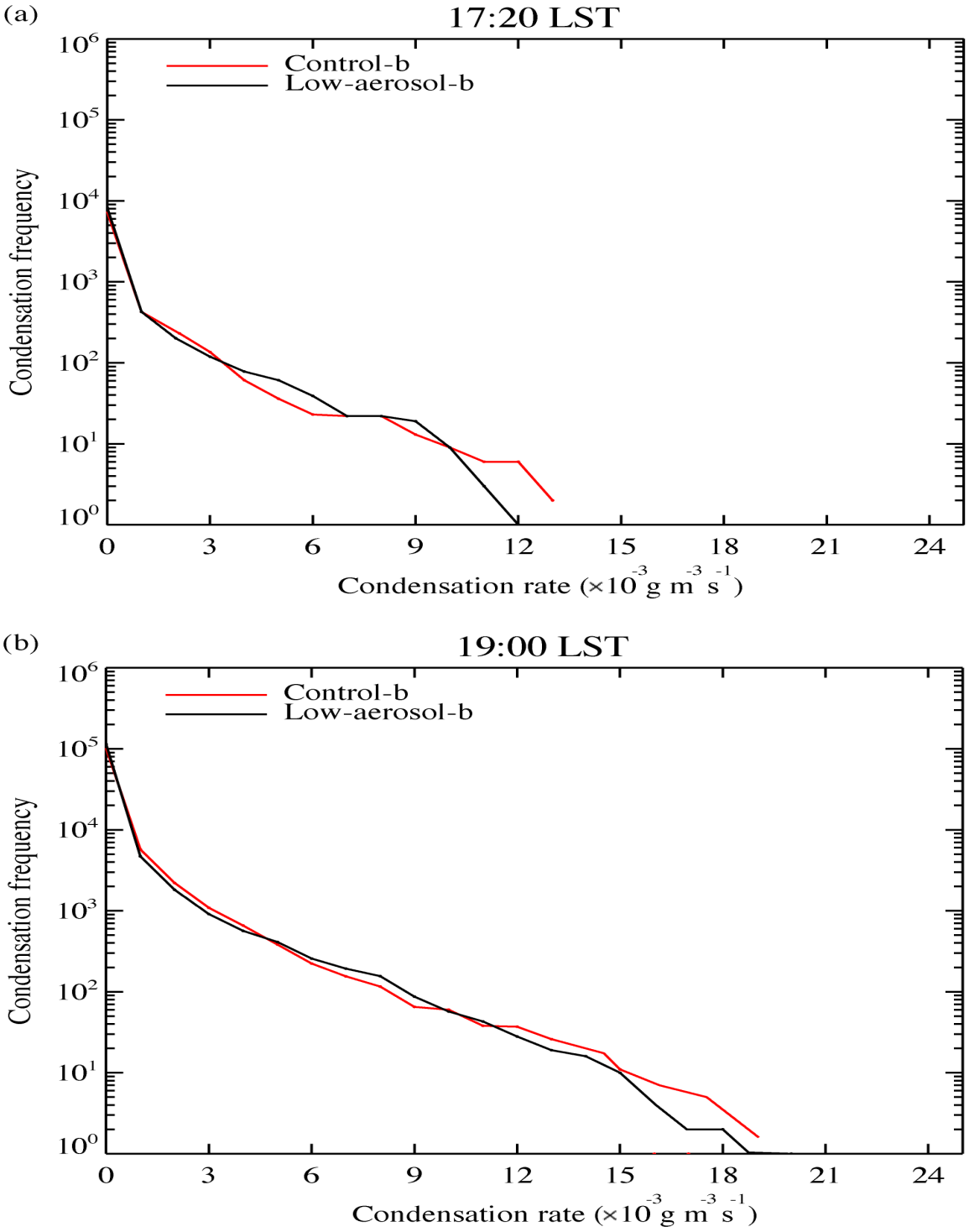

1337

1338 **Figure 14**

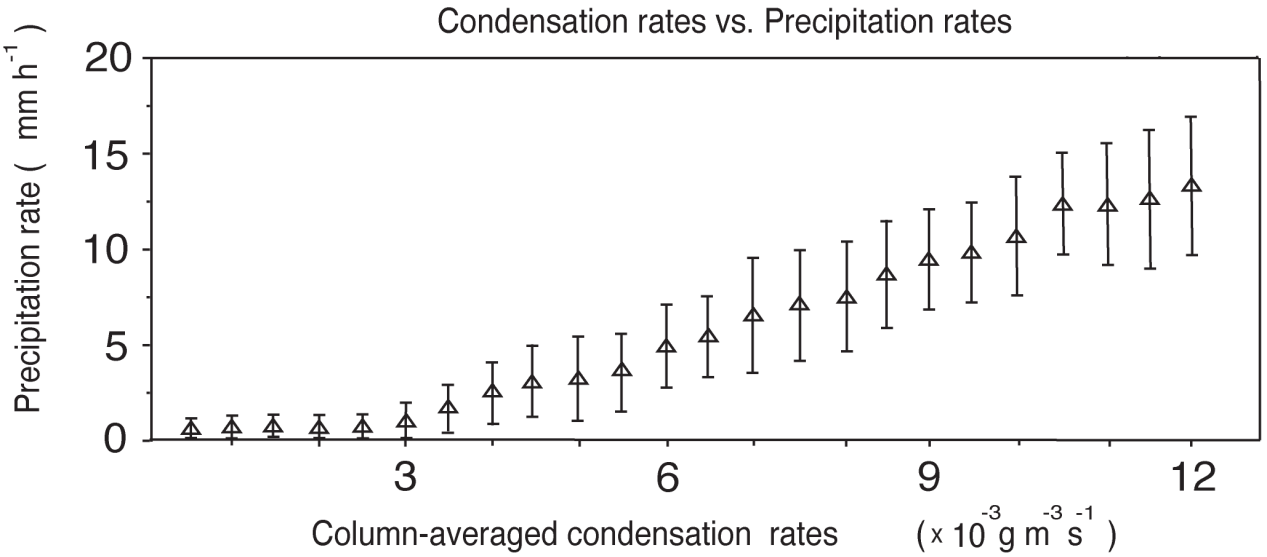
Condensation rates vs. Precipitation rates
Precipitation rate (mm h-1)
20
15
10
5
0
3
6
9
12
Column-averaged condensation rates (x 10-3 g m-3 s-1)

Figure 15

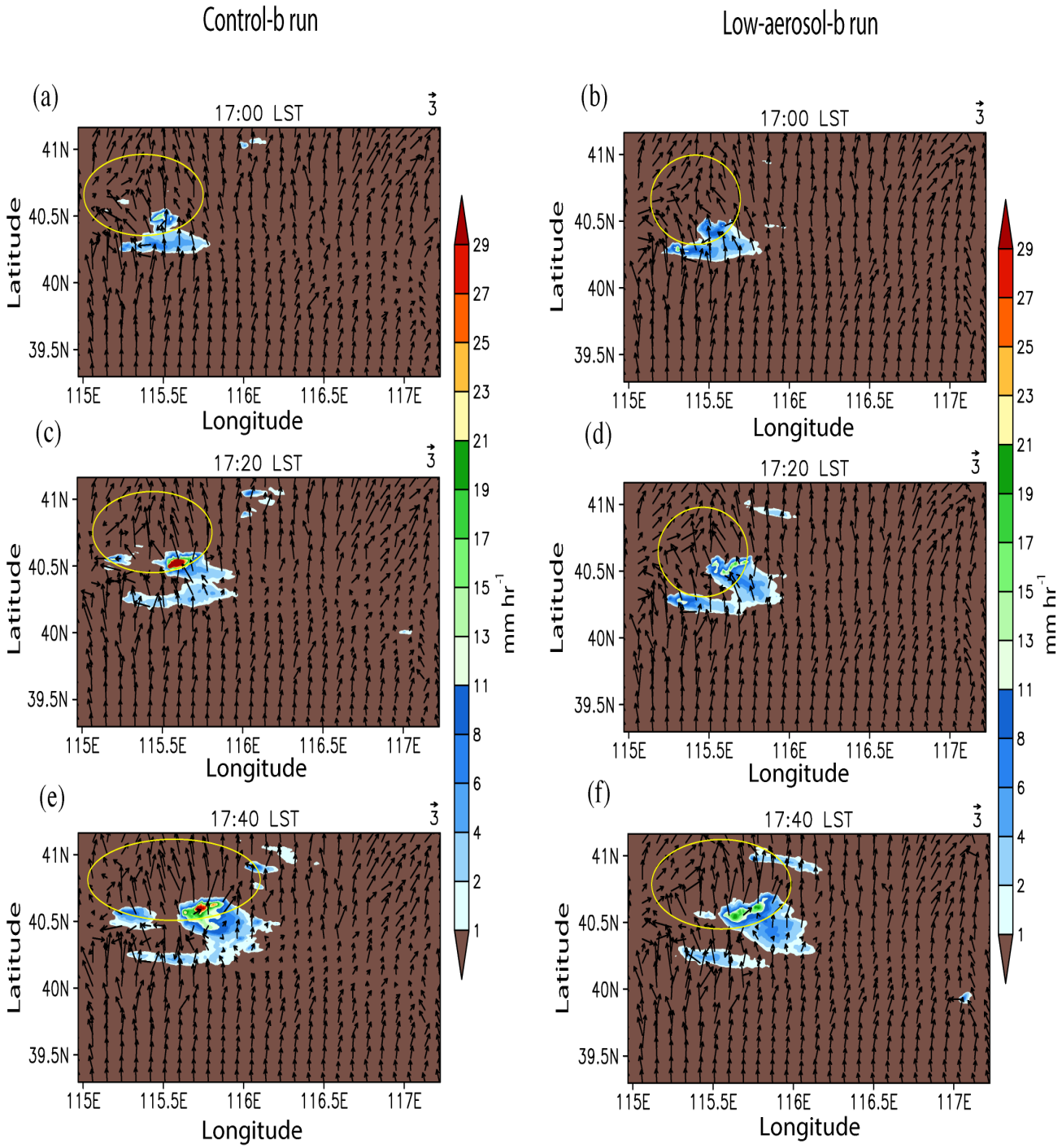
Control-b run
Low-aerosol-b run
(a)
17:00 LST
(b)
17:00 LST
(c)
17:20 LST
(d)
17:20 LST
(e)
17:40 LST
(f)
17:40 LST
Latitude
Longitude
41N
40.5N
40N
39.5N
115E
115.5E
116E
116.5E
117E
29
27
25
23
21
19
17
15
13
11
8
6
4
2
1
mm hr-1

Figure 16

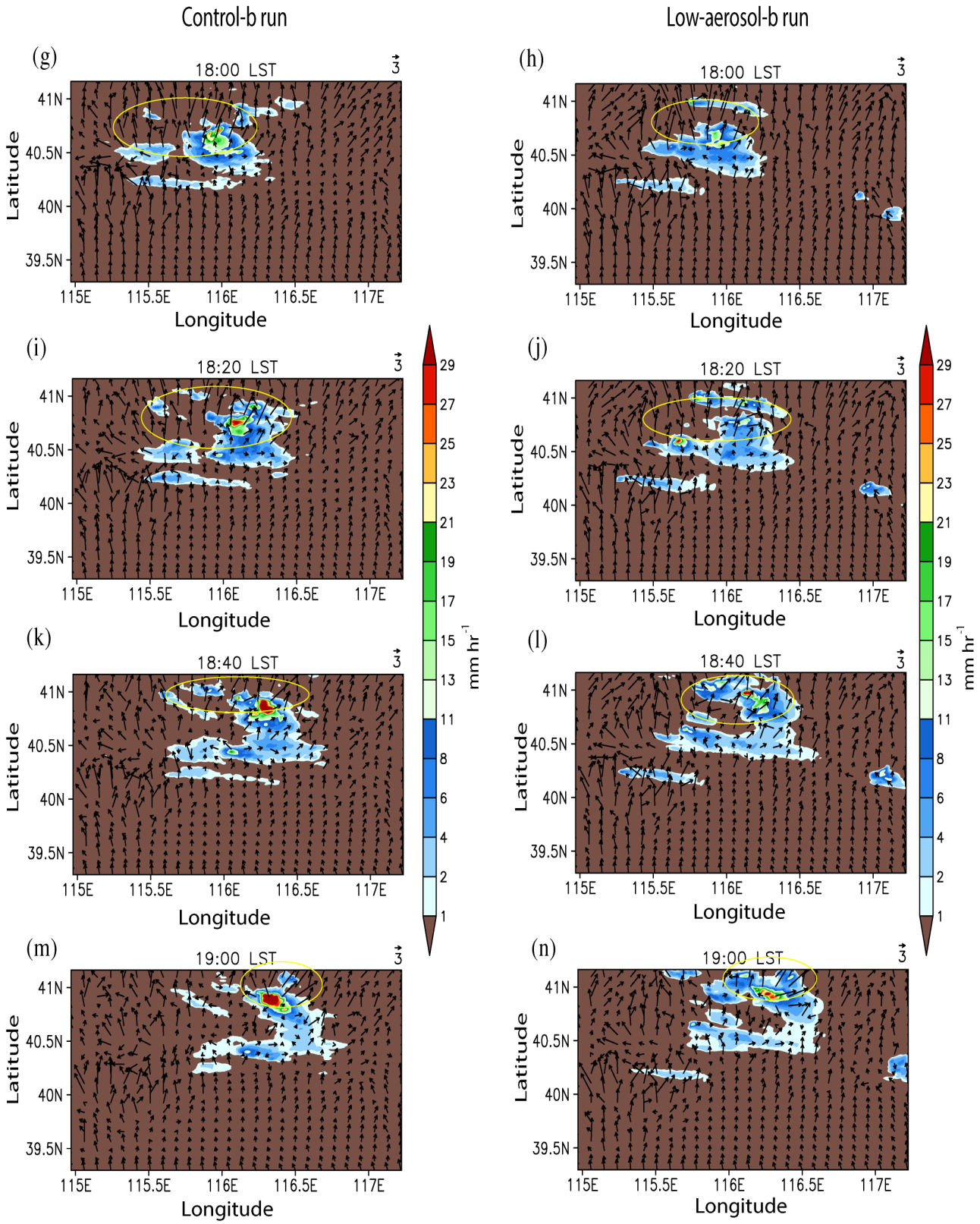

1355

1356 **Figure 16**

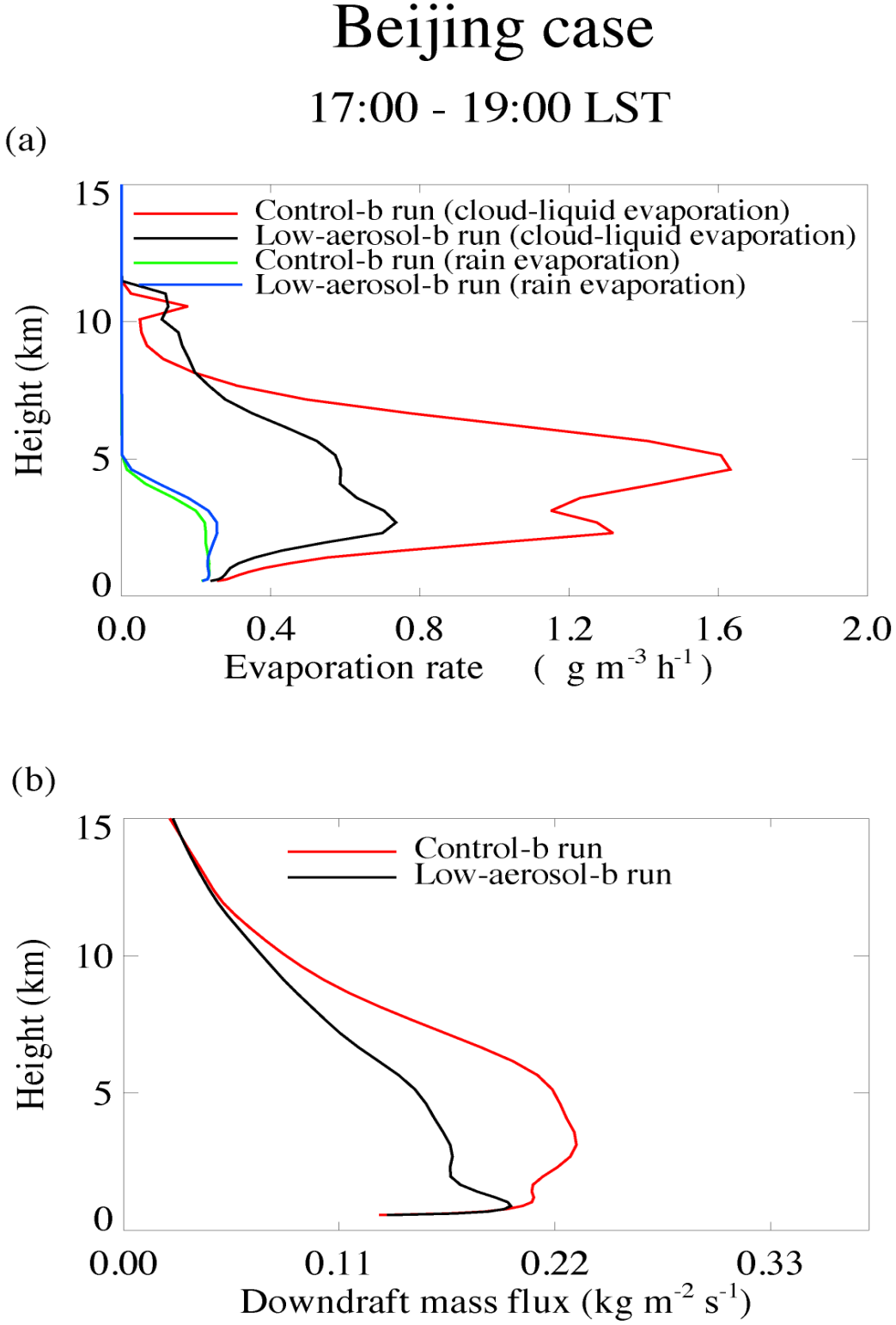

1357

1358 **Figure 17**

1359